Effects of Low-Level Flow Orientation and Vertical Shear on the Structure and Intensity of Tropical Cyclones

BUO-FU CHEN AND CHRISTOPHER A. DAVIS

National Center for Atmospheric Research, Boulder, Colorado

YING-HWA KUO

National Center for Atmospheric Research, and University Corporation for Atmospheric Research, Boulder, Colorado

(Manuscript received 15 December 2017, in final form 1 June 2018)

ABSTRACT

This article explores the simultaneous effect of vertical wind shear (VWS) and low-level mean flow (LMF) on tropical cyclone (TC) structure evolution. The structural evolution of 180 western North Pacific TCs from 2002 to 2014 was measured by a new parameter, the RV ratio, which is defined as the ratio of a TC's radius of 34-kt (17.5 m s^{-1}) wind to its maximum wind speed at the ending point of the intensification period. Whereas TCs with RV ratios in the lowest quartile of all 180 samples favored intensification over expansion, and 82% of these TCs experienced rapid intensification, TCs with RV ratios in the topmost quartile favored size expansion over intensification. A novel result of this study is that TC RV ratios were found to correlate with the LMF orientation relative to the deep-layer VWS vector. Specifically, whereas an LMF directed toward the left-of-shear orientation favors TC intensification, a right-of-shear LMF favors TC size expansion. This study further analyzed the TC rainfall asymmetry and asymmetric surface flow using satellite observations. Results show that for a TC affected by an LMF with right-of-shear orientation, the positive surface flux anomaly in the upshear outer region promotes convection in the downshear rainband region. On the other hand, a left-of-shear LMF induces a positive surface flux anomaly in the downshear outer region, thus promoting convection in the upshear inner core. Enhancement of the symmetric inner-core convection favors intensification, whereas enhancement of the downshear rainband favors expansion.

1. Introduction

The structure of a tropical cyclone (TC) can be described by a number of parameters associated with the TC tangential winds. Intensity, strength, and size are three such parameters documented by Holland and Merrill (1984). Intensity (i.e., the maximum sustained surface wind) is critically important because the wind-related damage of a TC is proportional to at least the square of the maximum surface wind. Zhai and Jiang (2014) estimated that the power relationship between wind speed and damage ranges between 4 and 12. On the other hand, strength (i.e., average wind in the 100–300-km radial band) and size (i.e., the radius of 34-kt wind; 1 kt = 0.5144 m s^{-1}) describe the outer vortex wind profile. Strength and size are important parameters for improving TC forecasts and warnings of wind damage (Powell and Reinhold 2007), storm surge (Irish et al. 2008), surface wave height (Sampson et al. 2013), and timing of the arrival of gale force winds (Stenger and Elsberry 2013). Also, Chan and Chan (2012) analyzed satellite-observed surface wind data and found that size is strongly correlated ($\Gamma = 0.9$) to strength.

An important feature of TC structure is that it develops with considerable variability. Maclay et al. (2008) documented that TCs generally either intensify and maintain their size, or they maintain their intensity and expand. Therefore, as TCs approach their maximum intensity, some become very large in size (R), while those remaining are moderate in intensity (V); others are very intense but only moderate in size. This diversity of TC structure development is also illustrated by a V–R diagram for 180 western North Pacific TCs (Fig. 1a). With any given intensity, TC size varies by approximately 150 n mi (1 n mi = 1.852 km).

Two examples show that forecasting TC structure development poses a challenge for TC warning and disaster management. First, Typhoon Haiyan (2013;

Corresponding author: Buo-Fu Chen, bfchen751126@gmail.com

DOI: 10.1175/MWR-D-17-0379.1

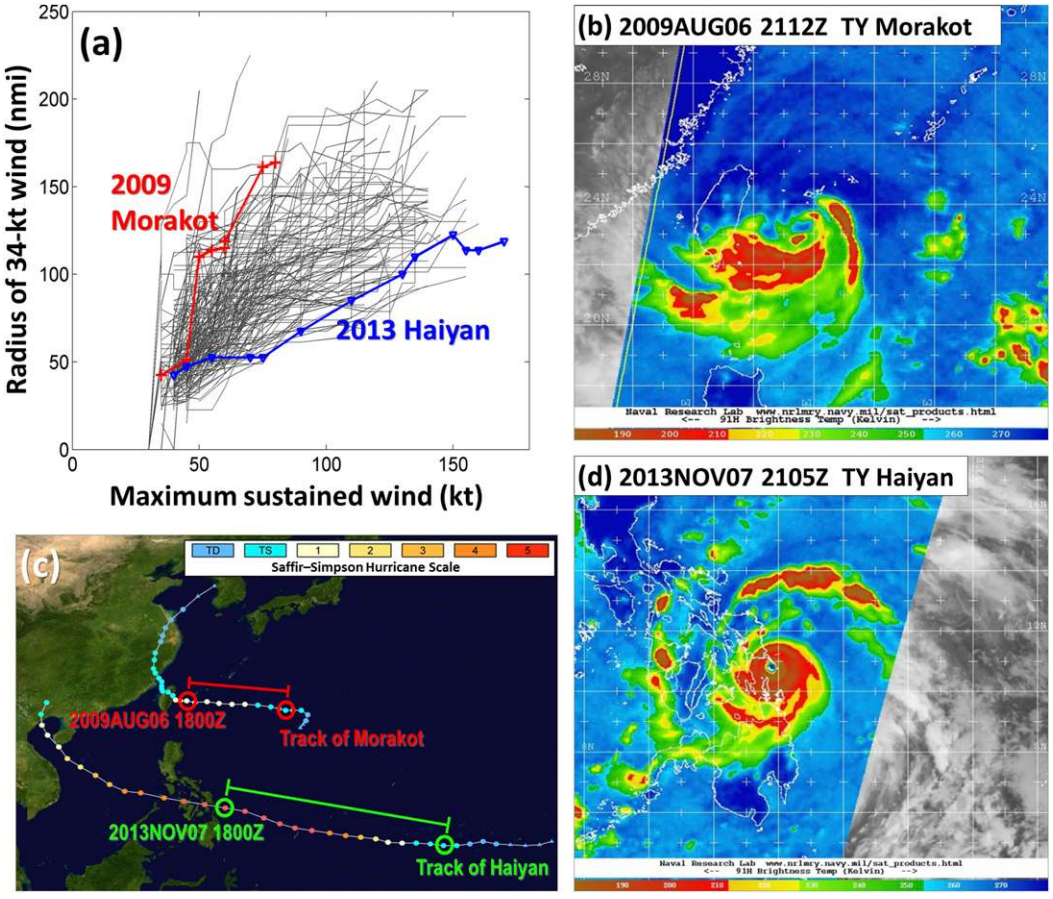

FIG. 1. (a) The *V*–*R* diagram of 180 western Pacific TCs during their intensification period. Typhoon Morakot (2009) is highlighted by the red line with crosses; Typhoon Haiyan (2013) is highlighted by the blue line with triangles. Both the crosses and triangles indicate 6-h intervals. (c) Tracks of Morakot and Haiyan, along which the intensification period [corresponding to (a)] are indicated by red and green lines. (b),(d) The 91-GHz horizontally polarized brightness temperatures near the time of (b) Morakot's and (d) Haiyan's peak intensities. Note that (b),(d) are from NRL TC webpage (http://www.nrlmry.navy.mil/TC.html).

highlighted in blue in Fig. 1a) experienced rapid intensification and reached a peak intensity of 170 kt with a moderate size of about 100 n mi. Second, Typhoon Morakot (2009; highlighted in red in Fig. 1a) reached its peak intensity of only 85 kt before making landfall in Taiwan with an anomalously large size of 200 n mi. Moreover, Morakot lacked well-organized inner-core convection but exhibited relatively asymmetric convection in the outer region (Fig. 1b), unlike Haiyan, which exhibited compact and well-developed inner-core convection (Fig. 1d). Therefore, the distinct structures of Haiyan and Morakot resulted in disastrous damage to society in different ways. Whereas the extreme wind gusts and storm surge within Haiyan's inner core resulted in severe damage in the Philippines, the strong outer circulation of Morakot contributed to catastrophic and unexpected rainfall in the TC outer region. This record-breaking rainfall in southern Taiwan—over 3000 mm in 3 days—was associated with active and sustained outer rainbands interacting with the steep topography (Lee et al. 2011, 2012).

Understanding how TC structure develops is also an important scientific issue because of the complicated and nonlinear underlying physical processes. Although the full extent of these processes has yet to be understood, TC structure development is known to be related to several environmental factors that serve as external forcings to the TC. These environmental factors include ocean heat content (Lin et al. 2013), upper-level outflow channels (Elsberry and Jeffries 1996), lower- to midtropospheric environmental relative humidity (RH; Hill and Lackmann 2009; Dunion and Velden 2004), and the vertical profile of background flows (Emanuel et al. 2004; Riemer et al. 2010; Rappin and Nolan 2012; see more details in the next paragraphs). To add to this critical work, this study explores

the relationships between TC structural development and two properties associated with the vertical profile of background flows: vertical wind shear and low-level environmental flow.

Vertical wind shear (VWS) is one of the most critical factors affecting TC intensification, structure changes, and predictability (Emanuel et al. 2004; Zhang and Tao 2013). DeMaria and Kaplan (1994, 1999) demonstrated that the magnitude of deep-layer (850–200 hPa) VWS is the leading predictor of TC intensity change. Emanuel et al. (2004) showed that VWS heightens the sensitivity of TC development to other environmental conditions. Furthermore, several studies have shown that VWS affects TC structure development by multiple physical processes, such as inducing asymmetric convective features (Frank and Ritchie 2001; Corbosiero and Molinari 2002, 2003; Hence and Houze 2011; Reasor et al. 2013; DeHart et al. 2014), venting moisture and energy out of the TC core (Tang and Emanuel 2010, 2012), and transporting low-entropy air into the inflow boundary layer (Riemer et al. 2010).

When a TC interacts with VWS, the asymmetrically balanced dynamics of the TC contribute to quasi-stationary convective asymmetry outside the eyewall. Specifically, the perturbation of the vortex by shear strongly projects onto a vertical and azimuthal wavenumber-1 vortex Rossby wave pattern (Reasor et al. 2004; Riemer et al. 2010), thereby resulting in an optimal vortex tilting orientation toward the downshear-left side (Jones 1995; Reasor et al. 2004). The resulting convective asymmetry has been attributed to the spiraling upward motion along the tilted isentropic surface and the increased convective instability within a wavenumber-1 moist envelope. Furthermore, in a recent study, Riemer (2016) proposed that asymmetric frictional convergence in the boundary layer associated with the wavenumber-1 asymmetric vorticity at the top of the boundary layer also contributes to the organization of the convection.

Although the fundamental processes associated with TC–VWS interaction have been extensively studied, and the predictability of the VWS relevant to a TC is documented to be over 1 week (Komaromi and Majumdar 2014), the predictability of TC intensification is still limited, in part due to the interactions between a TC and the vertically sheared background flows. In fact, recent idealized modeling studies have shown that in addition to the deep-layer VWS magnitude, considerable variability of the development and formation of simulated TCs arises from other factors, which include the relative orientation of the VWS to the surface wind (Rappin and Nolan 2012), the height and depth of vertical wind shear (Finocchio et al. 2016), and the environmental helicity (Onderlinde and Nolan 2014).

In addition to the VWS, low-level mean flow (LMF) also affects TC structure. First, the interaction between TCs and LMF may lead to frictional convergence in the boundary layer. Shapiro (1983) used a slab boundary layer model, forced by a prescribed wind field at the top of the boundary layer, to show that even without moist processes, the strongest convergence (and hence, vertical velocity in the slab model) occurs on the downstream side of the LMF with respect to the vortex. In full physical and idealized simulations, however, Thomsen et al. (2015) showed that this area of frictional convergence is shifted about 45° to the left of that predicted by Shapiro's model (Shapiro 1983) due to the modification of flow asymmetry at the top of the boundary layer by the asymmetric convection. In addition, the LMF also affects a TC by modifying the asymmetric low-level circulation and dividing the flow around the TC into distinct regions in which air flows either toward or away from the inner core (Riemer and Montgomery 2011). Finally, it has been proposed that TC rainbands may arise on the confluent boundary of storm circulation and the environmental LMF (Willoughby et al. 1984; Akter and Tsuboki 2012).

For western North Pacific TCs, several observational studies have shown that environmental LMF is related to TC structure and the development of organized and sustained rainbands (Liu and Chan 1999; Lee et al. 2010, 2012; Chen et al. 2014a). Based upon satellite wind observations, Liu and Chan (1999) and Lee et al. (2010) suggested that strong, low-level southwesterly monsoonal flow in summer, or strong trade wind surges in autumn, favors large TCs. Furthermore, Chen et al. (2014a,b) showed that a northeasterly VWS coupled with a strong LMF due to the southwest monsoon favors long-lasting and active TC rainbands. Moreover, these long-lasting rainbands were associated with higher TC expansion rates and less intensification. Recalling the example of Typhoon Morakot (2009), the dramatic size expansion of Morakot (Fig. 1a) was actually accompanied by several long-lasting rainbands associated with the TC–monsoon interaction. These long-lasting rainbands are connected with the TC inner core and present a large, cold cloud shield lasting over 6 h (Fig. 1b provides a snapshot of this kind of rainband). Note, however, that neither the physical process underlying the formation of these long-lasting rainbands associated with southwesterly LMF nor the feedback from these rainbands on TC structure is fully understood.

TC structure development is characterized by considerable variability, and the pathway of structural evolution to some extent is attributed to the effects of VWS and LMF. However, our knowledge and the predictability of TC structure development remains limited

due to a lack of understanding of the nonlinear processes between a TC and the vertically sheared background flows. Therefore, the current paper explores TC structural development by examining the simultaneous effects of both VWS and LMF. While this approach may lead to more complicated analyses and perhaps results that are more difficult to interpret, it can supply valuable information unavailable with a conventional approach that deals with only one factor at a time.

In light of the foregoing, the methodology for this study involves a systematic examination of the relationship between TC structure development and the VWS and LMF for western Pacific TCs. Also, possible explanations for the tendency of a TC to intensify or expand under the effects of VWS and LMF are addressed. In the next section, the data and methodology are described. Section 3 explores the relationship between TC structural evolution and several environmental factors, with emphasis on the role of the shear-relative LMF. Section 4 examines the composites of satellite rainfall and surface wind data to address physical processes that affect the structure of TCs influenced by the shear-relative LMF. The final section offers concluding remarks and suggestions for future work.

2. Data and methodology

This section first introduces a new parameter, the RV ratio, to describe TC structure evolution (section 2a). Second, the calculation of the environmental VWS and LMF is described. Then, rotated-LMF, a new parameter measuring the LMF with respect to the VWS, is introduced (section 2b). Finally, section 2c describes the data and calculation for composite analyses used to explore the physical processes affecting TC structure.

a. Calculating the RV ratio

In this study, TC intensity and size were obtained from Joint Typhoon Warning Center (JTWC) best track data. These files contain TC information including latitude, longitude, 1-min maximum sustained surface wind, and central pressure at 6-h intervals for TCs occurring since 1945. After August 2001, JTWC began providing maximum radial extent by quadrant of 34-, 50-, and 65-kt winds and other structure metrics by taking advantage of advanced analysis techniques and modern satellite remote sensing (e.g., wind speeds observed by Special Sensor Microwave/Imager and surface wind vectors observed by the scatterometer on QuikSCAT). In addition to the size of the wind field, other structure metrics are also included: the radius of maximum wind, the eye diameter, and the radius of the outermost closed isobar. However, in addition to the intensity, the current study focuses on the size of 34-kt winds because it is vital to disaster warning/management and in determining storm-related impacts, such as the areas impacted by destructive winds and storm surges.

To estimate the tendency of a TC to intensify or expand, a new parameter, the RV ratio, was calculated. A total of 180 TCs from 2002 to 2014 are included in the analyses. The RV ratio is defined as the ratio of a TC's intensity (V) and size (R) at the ending point of the intensification period, where V is the 1-min maximum sustained surface wind speed, and R is the average of the radii of 34-kt winds in all four quadrants. In addition, the TC intensification period is defined as the period that begins when the R is first available and ends when the TC exhibits the highest intensity prior to the first pronounced weakening of at least 10 kt in 6 h. In our dataset, most of the TCs (159/180) reached their lifetime maximum intensity at the ending point of the intensification period. However, some of the TCs (21/180) exhibited pronounced weakening due to crossing Luzon and Taiwan. Thus, for these TCs, the intensification periods were terminated just before landfall. Furthermore, the duration of the intensification period is required to be greater than 24 h. Figure 2a shows the 180 TCs' V and R at their ending point of the intensification period. The slope of a line from the grid origin to the point of any TC is the RV ratio.

As shown in Fig. 2a, the 180 TCs were divided into four quartiles of the distribution by the RV ratios. For example, the TCs in the first quartile (0–25th percentile) had RV ratios less than 0.93 n mi kt^{-1}, whereas the TCs in the uppermost quartile (75th–100th percentile) had RV ratios larger than 1.47 n mi kt^{-1}. Although the RV ratios were calculated using a single datum taken at the ending point of the intensification period, the RV ratios are consistent with the rate of TC intensification and size expansion during the intensification period (Figs. 2b,c). Therefore, the RV ratio could represent the pathways of TC structural development. Namely, whereas a TC with a small RV ratio had a larger intensification rate and a smaller expansion rate, a TC with a large RV ratio exhibited the converse relationship (Figs. 2b,c). As a result, if a TC had experienced rapid intensification (RI; Kaplan and DeMaria 2003), it had a higher chance of exhibiting a small RV ratio. Following Kaplan and DeMaria (2003), RI is defined as the intensification $\geq$30 kt during any 24-h interval. Although the 30-kt threshold is consistent with the 95th percentile of overwater intensity change for Atlantic TCs (Kaplan and DeMaria 2003), it is consistent with the 69th percentile of the samples during the intensification periods of the 180 western Pacific TCs in this study. Thus, 106 of the 180 TCs (59%) are RI cases, and 82%, 73%, 51%, and

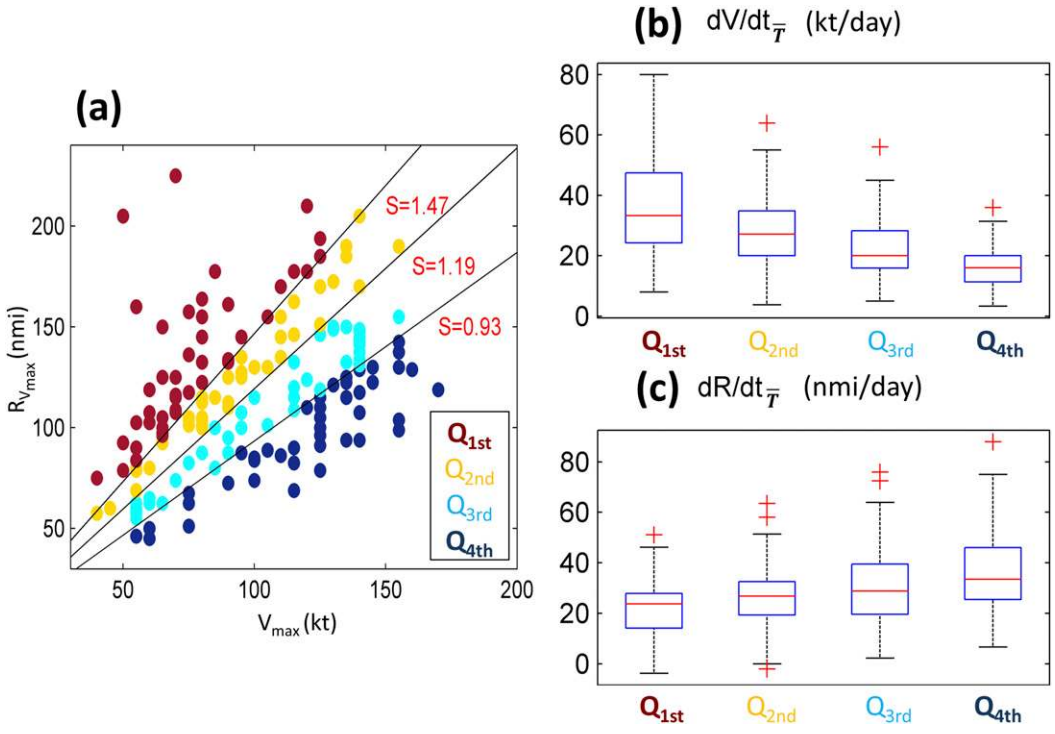

FIG. 2. (a) The scatterplot of V and R at the ending point of the intensification period for 180 TCs. TCs having RV ratios in different quartiles of the distribution are indicated by dark blue, sky, gold, and brown spots. Lines and the RV ratios (red text) dividing those four quartiles are also drawn. Boxplots of (b) averaged intensification rates and (c) averaged size expansion rates of each TC for the four quartiles. In each box, the median and the 25th (q1) and 75th (q3) percentiles are indicated; the whiskers extend to the most extreme data points not considered outliers; and the + symbols indicate outliers that are greater than q3 + 2.7σ or less than q1 − 2.7σ, where σ is the standard deviation.

28% of TCs in various quartiles of the RV ratios exhibited RI.

b. *Calculating VWS, LMF, and other environmental factors*

Examination of the factors affecting TC RV ratios relied upon the National Centers for Environmental Prediction (NCEP) Final (FNL) operational global analyses (i.e., NCEP-FNL) on a 1° × 1° grid. Although the coarse resolution of NCEP-FNL presents the difficulty of measuring any parameters associated with a TC vortex, NCEP-FNL is sufficient to calculate environmental factors, such as background flow, environmental relative humidity,[1] and sea surface temperature (SST).[2]

In this study, VWS is defined as the difference between 200- and 850-hPa mean flows, with LMF as the 850-hPa mean flow. The environmental mean flows at 200 and 850 hPa were calculated following the methodology described in Davis et al. (2008) and Galarneau and Davis (2013). Briefly, this methodology removes both the rotational and divergent winds associated with a TC vortex within 5° of the TC center. Then, the mean flow at each level can be computed as the average in the 5° circular area. Thus, this methodology has a better tolerance to TC location error than the conventional method, which is based upon the areal average without removing vortex flows.

To examine the simultaneous effects of the VWS and the LMF on the RV ratio, the second parameter introduced in this study is the rotated LMF (LMF_{rot}), which is defined as the LMF on a rotated coordinate relative to the VWS vector. A schematic of a rotated VWS vector and four corresponding LMF_{rot} vectors are shown in Fig. 3d.

Some statistical characteristics and the seasonal variations of the averaged VWS and LMF_{rot} during the

[1] There may be significant biases of humidity, but the present study is mainly concerned with differences among samples.

[2] We have compared the results based on NCEP-FNL sea surface temperature and NOAA Optimum Interpolation sea surface temperature. The usages of different datasets do not significantly change the statistical results in this study.

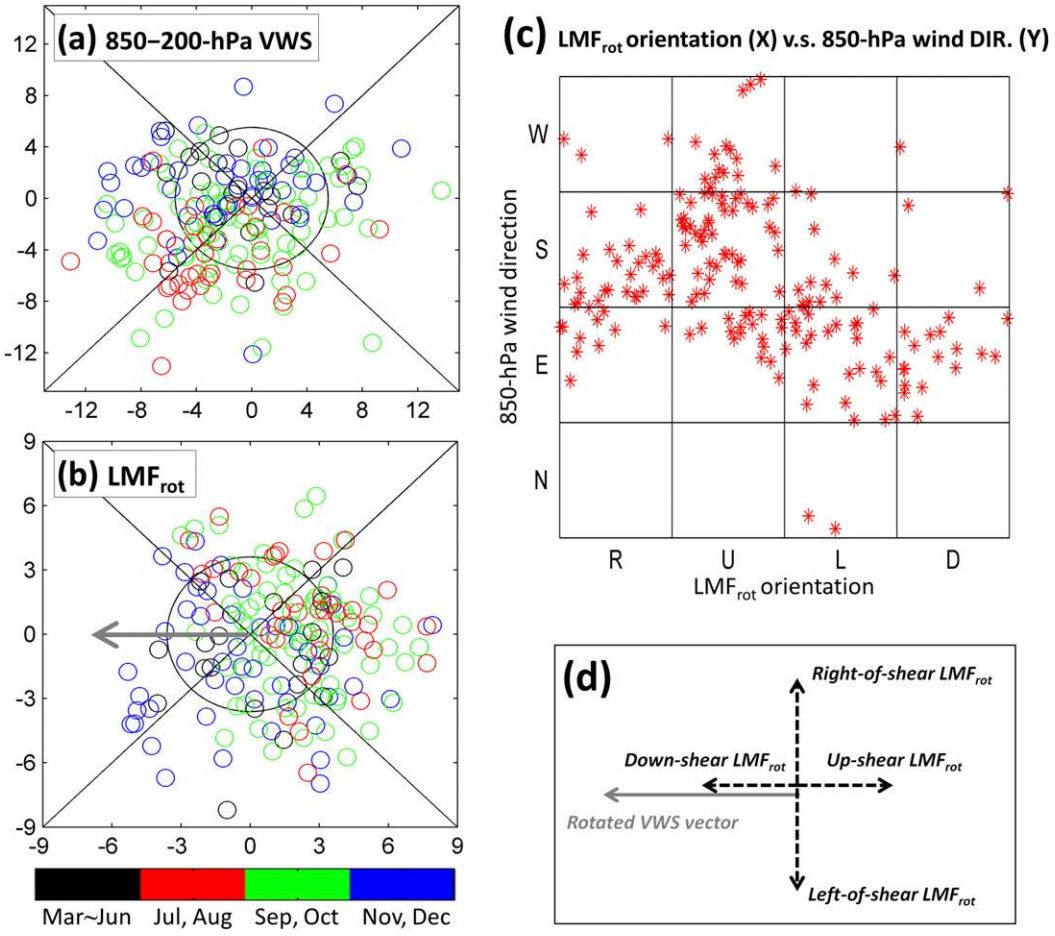

FIG. 3. (a) Scatterplot of the eastward velocities (x axis; m s^{-1}) and northward velocities (y axis; m s^{-1}) of averaged VWS vectors of the 180 TCs during their intensification period. The occurrence month of each TC is indicated by the color bar. (b) As in (a), but for averaged LMF$_{rot}$ vectors of the 180 TCs during their intensification period. Note that in (b), every LMF$_{rot}$ is plotted on the rotated coordinate in which the VWS vector is rotated toward the west (gray arrow). (c) Scatterplot of LMF$_{rot}$ orientations (x axis) and 850-hPa mean flow directions (y axis) of the 180 TCs; R, U, L, and D indicate right of shear, upshear, left of shear, and downshear, respectively, and S, W, N, and E indicate south, west, north, and east, respectively. (d) The schematic of a rotated VWS vector and four corresponding LMF$_{rot}$ vectors.

intensification period for the 180 TCs were examined. As shown in Fig. 3a, TCs more frequently experienced westerly (73/180) or northerly (50/180) VWS than easterly (35/180) and southerly (22/180) VWS. Furthermore, the mean of southerly VWS magnitudes (3.3 m s^{-1}) was weaker than that of VWS with other orientations (ranging from 5.5 to 6.1 m s^{-1}). On the other hand, the median of LMF$_{rot}$ experienced by a TC is 3.6 m s^{-1}, though LMF$_{rot}$ magnitudes were larger in July and August (red circles in Fig. 3b). These larger LMF$_{rot}$ magnitudes may be associated with the southwesterly monsoonal flow. Also, 22% of the 180 LMF$_{rot}$ vectors had right-of-shear orientations, 43% oriented toward upshear, 23% oriented toward left of shear, and 12% oriented toward downshear.

TCs in July and August (red circles in Figs. 3a,b) frequently experienced northeasterly VWS (VWS vectors point toward the southwest) with upshear-right LMF$_{rot}$, whereas TCs in the early and late portions of the season (black and blue circles in Figs. 3a,b) were more likely to experience southerly VWS with downshear-left LMF$_{rot}$. Finally, Fig. 3c shows that TCs with upshear LMF$_{rot}$ orientations usually experienced southerly and westerly LMF, whereas TCs affected by downshear LMF$_{rot}$ orientations were likely to experience easterly LMF. Note that only two TCs were affected by northerly LMF. These results suggest that the VWS–LMF configuration appears to be associated with the different synoptic environments in different seasons. This argument is further examined in section 3c.

c. Using satellite observations to elucidate the physical processes associated with TC–LMF$_{rot}$ interaction

To explore the physical processes associated with the effects of LMF$_{rot}$ on a vertically sheared TC, this study utilized composite analyses to examine the wind and convection asymmetry based on satellite data, including precipitation rates obtained by the Climate Prediction Center morphing technique (CMORPH; Joyce et al. 2004) and oceanic wind observations from the QuikSCAT satellite.

CMORPH precipitation rates from 2003 to 2014 were used to conduct composites to investigate rainfall asymmetries associated with TCs interacting with various LMF$_{rot}$ orientations. The CMORPH uses precipitation estimates derived from low-orbit microwave satellite observations exclusively, whose features are transported via spatial propagation information obtained entirely from geostationary satellite IR data. Since the resolution of rain rate estimated by individual satellite is on the order of about 12 km × 15 km, the CMORPH data are available at 0.25° resolution every 3 h.

To create CMORPH composites, the CMORPH rain-rate field within a 10° radius of the TC center at each synoptic time (i.e., 0000, 0600, 1200, and 1800 UTC) during the intensification period was rotated to fit in a shear-relative coordinate. Second, each of the 180 TCs was classified into one of four subgroups according to the averaged LMF$_{rot}$ orientation during the intensification period (i.e., right of shear, upshear, left of shear, and downshear). Finally, the composites of rotated CMORPH precipitation rates for the four LMF$_{rot}$ orientations are constructed from samples during the intensification periods of the TCs associated with various LMF$_{rot}$ orientations.

This study also examines the surface wind associated with TCs during 2003–09 for those times with available QuikSCAT observations. The QuikSCAT dataset was prepared by Remote Sensing Systems with a geophysical model function called Ku-2011 (Ricciardulli and Wentz 2015). The SeaWinds instrument on the QuikSCAT satellite was a specialized microwave radar that measured near-surface wind speed and direction under all weather and cloud conditions over Earth's oceans. Although the resolution of QuikSCAT data is about 25 km, and the scatterometer may underestimate high wind speeds associated with a TC's inner core, it has been shown that QuikSCAT data are sufficient to investigate TC size changes and outer wind structure (Lee et al. 2010; Chan and Chan 2012).

To construct QuikSCAT composites, QuikSCAT surface wind vectors within a 10° radius of the TC center were first rotated to fit in the shear-relative coordinate. Next, these QuikSCAT observations are classified into four subgroups based on the LMF$_{rot}$ at the closest synoptic time from the observation. Finally, QuikSCAT composites for the four groups of TCs interacting with right-of-shear, upshear, left-of-shear, and downshear LMF$_{rot}$ were created.

3. Analyses of TC structural development described by the RV ratio

a. The relationship between RV ratios and several environmental factors

As previous studies have shown that TC structural development is related to the environment where the TC is embedded (e.g., Lin et al. 2013; Hill and Lackmann 2009; Dunion and Velden 2004; Emanuel et al. 2004; Riemer et al. 2010; Rappin and Nolan 2012), this subsection first explores the relationships between the RV ratios and several environmental factors (Fig. 4). As shown in Fig. 4a, the mean TC latitude during the intensification period is positively correlated with the RV ratio. This result is consistent with that of the numerical modeling study of Chan and Chan (2014): a larger planetary vorticity favors a larger TC size. However, changes in latitude may be also associated with different thermodynamic conditions, such as the sea surface temperature, and different synoptic background flow. Figure 4b shows that the RV ratio is also correlated with the TC size when it was first recorded in the JTWC best track data. This result agrees with previous studies (Chan and Chan 2014, 2015) showing that large initial vortex size favors size expansion.

Figures 4c and 4d examine the correlations of environmental SST and RH with the RV ratio. The environmental SST is represented by the averaged SST in a 2°–5° radial ring with respect to the TC center through the entire intensification period, while the environmental RH is represented by the averaged 700–850-hPa RH in a 2°–8° radial ring through the entire intensification period. Although these two environmental factors both exhibit significant positive correlations with both the TC intensification rate and size expansion rate (not shown), the correlations of both the SST and the RH with the RV ratio are not significant.

However, a larger averaged VWS magnitude during the intensification period significantly correlates with a larger RV ratio (Fig. 4e). This correlation is hypothesized to occur since there is a significant negative correlation of the VWS magnitude with TC intensification, while there is no correlation with size expansion (not shown). Also, there are no significant correlations

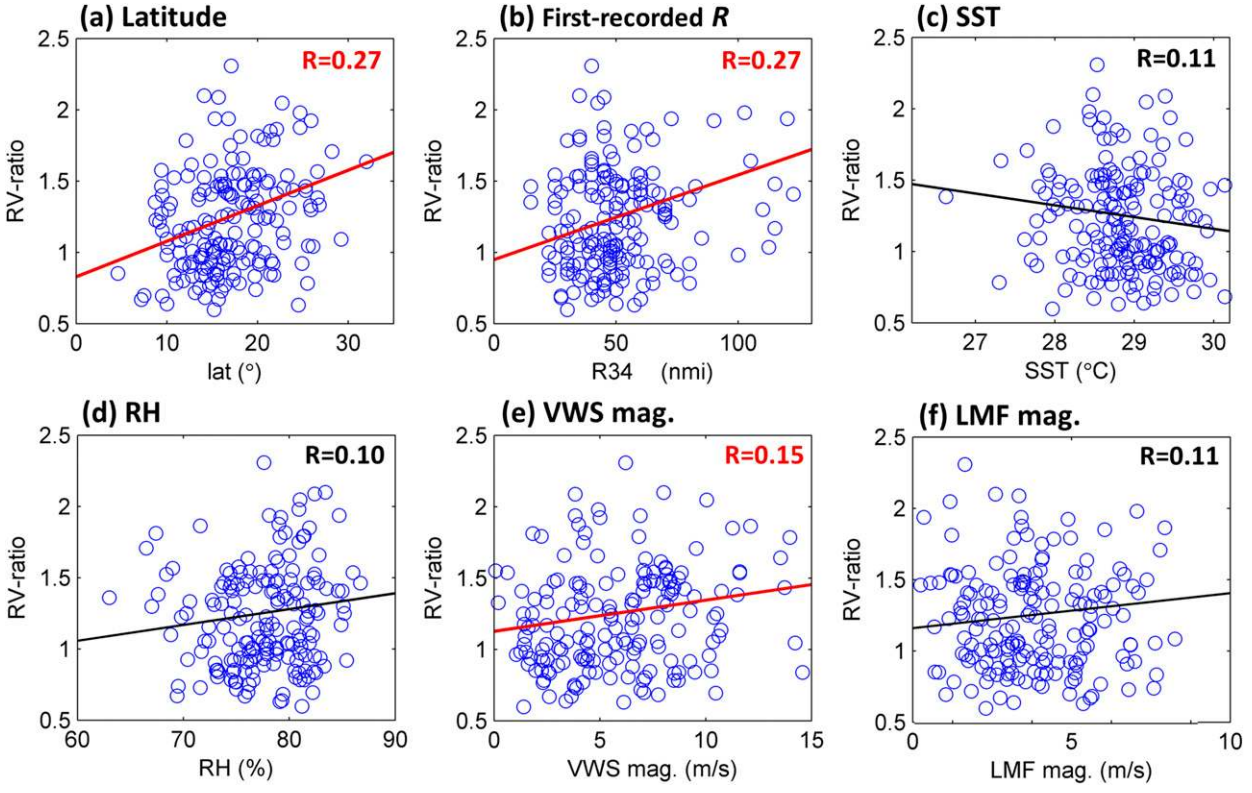

FIG. 4. Scatterplots of the RV ratios vs six environmental (or TC) parameters: (a) latitude, (b) the first available R, (c) environmental SST, (d) environmental RH, (e) VWS magnitude, and (f) magnitude of LMF_{rot}. The least squares regression line and correlation coefficient (R=) are shown. The red color in (a)–(c) indicates that these corrections are significant at the 95% confidence level according to the P values of Pearson correlation.

between the RV ratio and LMF magnitude (Fig. 4f), TC translation speed (not shown), and VWS direction (not shown).

b. *Examinations of the relationship between the LMF_{rot} orientations and the RV ratios*

It is most notable that the RV ratio also displays a strong relationship with the LMF_{rot} orientation (Fig. 5). This relatively new factor proposed to affect TC structure is somewhat similar to the shear-relative surface flow orientation investigated by Rappin and Nolan (2012). In their idealized simulations, an upshear/downshear shear-relative surface flow was prescribed by adding/removing a $3\,m\,s^{-1}$ mean flow at every level to a $5\,m\,s^{-1}$ deep-layer westerly VWS; thus, an upshear/downshear shear-relative surface flow is expected to be associated with a shear-relative LMF with the same orientation. They also show that an upshear shear-relative surface flow favors TC intensification. The distributions of the RV ratios for four subgroups of LMF_{rot} directed toward right of shear (R), upshear (U), left of shear (L), and downshear (D) are shown in Fig. 5a. If a TC is affected by a right-of-shear LMF_{rot} during the intensification period, it tends to have a larger RV ratio than that of a TC affected by a left-of-shear LMF_{rot}. To evaluate the statistical significance of the results, a Student's t test was used to test whether the difference between the mean of all 180 samples and the mean of each group is significant. Furthermore, a Kolmogorov–Smirnov test was also applied to confirm that the distribution of each group does not significantly differ from the Gaussian distribution and, thus, is suitable for the t test. The significance tests show that the mean RV ratio (1.33) of the right-of-shear LMF_{rot} is significantly larger than the mean RV ratio (1.21) of all 180 TCs at the 95% confidence level, while the mean RV ratio (1.06) of the left-of-shear LMF_{rot} is significantly less than the all-sample mean (1.21).

As TC structural evolution is clearly a multivariate problem, it is important to demonstrate that the relationship between the RV ratios and the LMF_{rot} orientations is not coincidently attributed to the correlation of the LMF_{rot} orientations with other environmental factors. Figures 5b–e show that except for the SST (Fig. 5c), no significant differences in VWS magnitude (Fig. 5b), environmental RH (Fig. 5d), and latitude

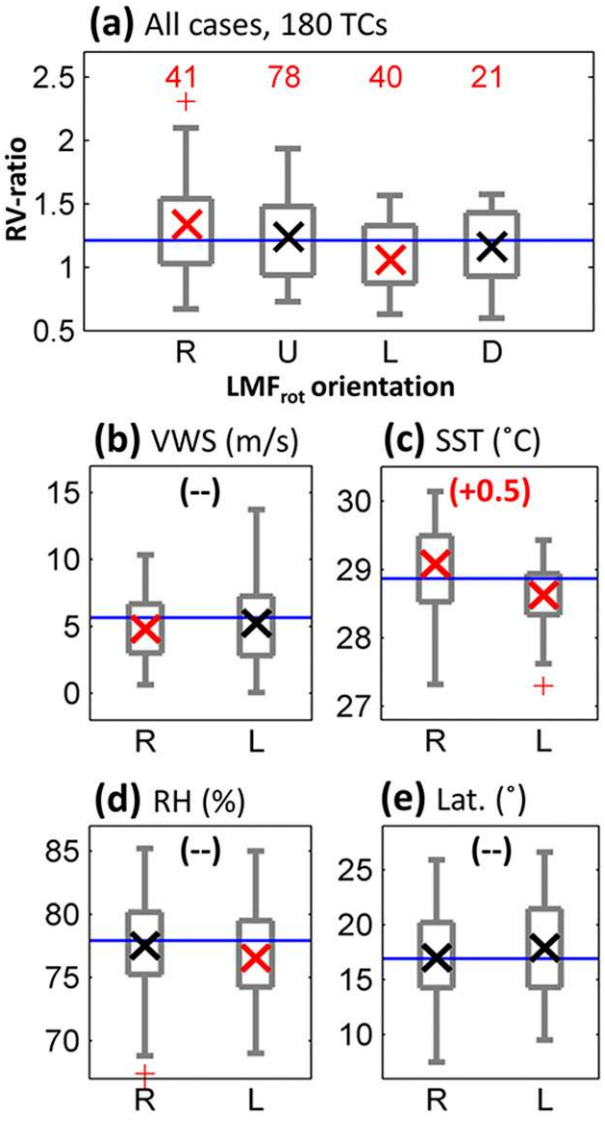

FIG. 5. (a) Boxplots of RV ratios for TCs affected by the four LMF$_{rot}$ orientations (i.e., R, U, L, and D). All 180 TCs are included, and the red font indicates the sample sizes of each group. In each box, the mean and the 25th (q1) and 75th (q3) percentiles are indicated; the whiskers extend to the most extreme data points not considered outliers; and the + symbol indicates outliers that are greater than q3 + 2.7σ or less than q1 − 2.7σ, where σ is the standard deviation. The horizontal blue line indicates the mean of all samples, and the red (black) × represents that the mean of a group larger or less than the mean of all samples at the 95% (not significant) confidence level. (b)–(e) As in (a), but for (b) VWS magnitudes, (c) SST, (d) RH, and (e) latitudes during the intensification period for TCs affected by right-of-shear and left-of-shear LMF$_{rot}$ orientations. The red text in (c) indicates the mean difference between these two groups, which is significant at the 95% confidence level according to a two-sample *t* test.

(Fig. 5e) are found between the right-of-shear and left-of-shear subgroups. Recall in Fig. 4 that both the VWS magnitude and latitude show positive correlations with the RV ratio; however, analyses here suggest that the relationship between the RV ratio and the LMF$_{rot}$ orientation could not be attributed to the difference in either the latitude or the VWS magnitude. On the other hand, although the SST is significantly higher for the right-of-shear subgroup (Fig. 5c), it is the opposite of what one would expect based on the well-known positive correlation of intensity with SST. These results indicate the importance of the LMF$_{rot}$ orientation on TC structural evolution beyond an environmental relationship and motivate the search for the physical processes associated with the effect of shear-relative LMF on TC structure discussed later in section 4.

To further explore the effect of VWS magnitude on the relationship between the RV ratio and the LMF$_{rot}$, Figs. 6a and 6b show the means and box plots of the RV ratios for the four LMF$_{rot}$ groups for strongly (>5.5 m s^{-1}; Fig. 6a) and weakly (<5.5 m s^{-1}; Fig. 6b) sheared TCs. It again shows that the average of the RV ratios for left-of-shear LMF$_{rot}$ is significantly smaller than the all-sample mean at the 95% confidence level for both the weak and strong VWS. On the contrary, right-of-shear LMF$_{rot}$ is associated with larger RV ratios for TCs in relatively weak VWS (Fig. 6b). Note also that the samples in the uppermost quartile (whiskers above the boxes in Fig. 6) of the right-of-shear LMF$_{rot}$ had much larger RV ratios (greater than 1.5). For downshear LMF$_{rot}$, the strong VWS subgroup exhibits significantly larger RV ratios, while the weak VWS subgroup exhibits significantly smaller RV ratios. To further evaluate the statistical difference between TCs affected by LMF$_{rot}$ with various orientations, two-sample *t* tests were applied. The results of the *t* tests suggest that for both the weak VWS (Table 1) and the strong VWS (Table 1), the mean RV ratio of right-of-shear LMF$_{rot}$ is significantly larger than that of left-of-shear LMF$_{rot}$ at the 95% confidence level. Note that these results of two-sample *t* tests also suggest that TCs affected by upshear LMF$_{rot}$ tend to exhibit RV ratios similar to those of the right-of-shear LMF$_{rot}$ cases and significantly larger than the RV ratios of left-of-shear LMF$_{rot}$ cases.

By definition, the RV ratio is affected by either *V* or *R* of a TC. Thus, Figs. 6c–f examine the averaged intensification rate and averaged expansion rate during the intensification period for TCs interacting with various LMF$_{rot}$ orientations under weak and strong VWS. For TCs affected by strong VWS (Figs. 6c,e), right-of-shear LMF$_{rot}$ favors higher size-expansion rates (significantly larger than the mean of all samples at the 90% confidence level; the green X in Fig. 6c) and moderate intensification rate, whereas left-of-shear LMF$_{rot}$ favors lower size-expansion rates (Fig. 6c) and higher intensification rates (Fig. 6e). On the other hand, for the weak VWS subgroup (Figs. 6d,f), the relationship between the

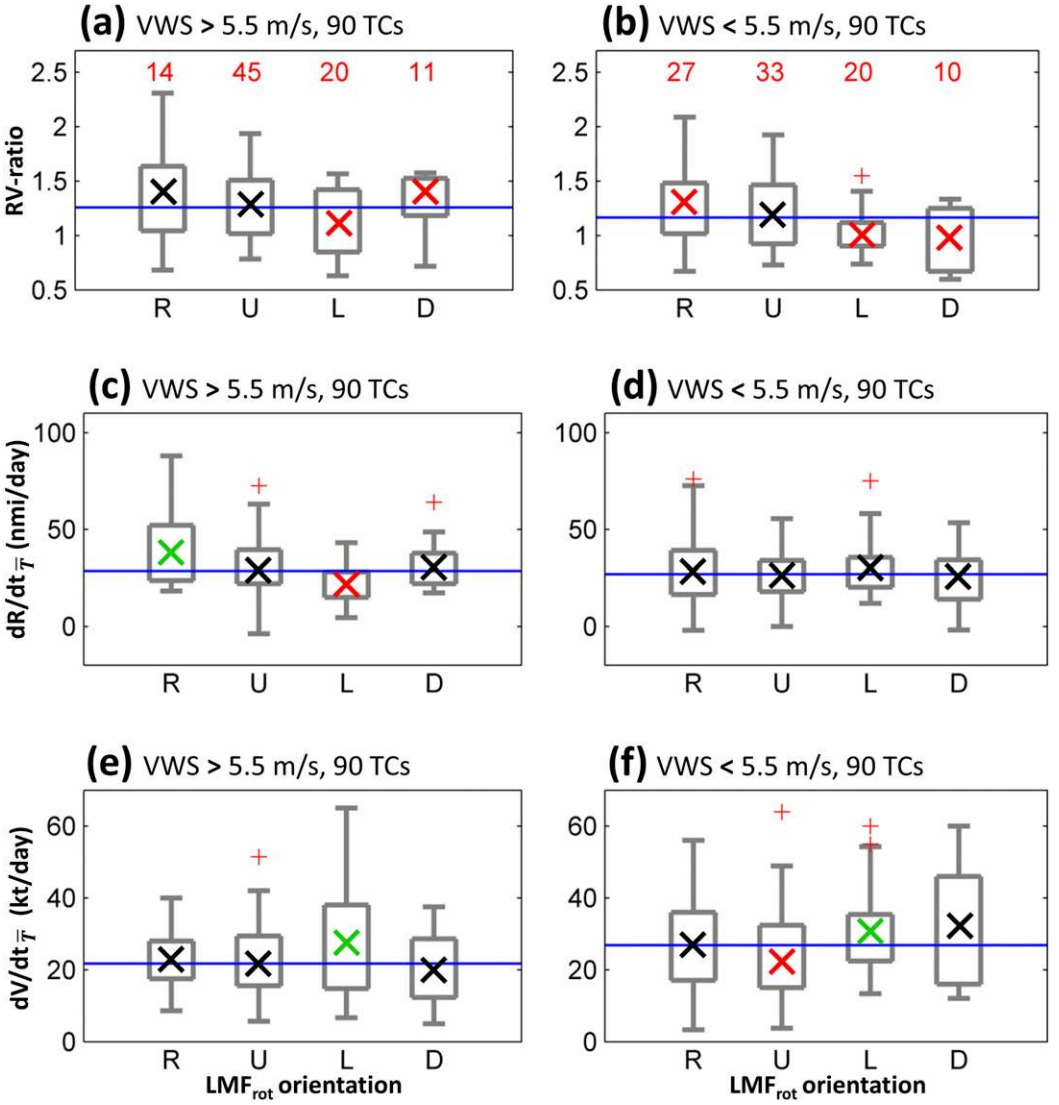

FIG. 6. As in Fig. 5a, but the boxplots of three TC structural parameters are for TCs affected by the four LMF_{rot} orientations (i.e., R, U, L, and D) under two conditions: (a),(c),(e) VWS magnitudes $> 5.5\ m\ s^{-1}$; (b),(d),(f) VWS magnitudes $< 5.5\ m\ s^{-1}$. These three structural parameters are (a),(b) RV ratios; (c),(d) averaged size expansion rates during the TC intensification periods [$dR/dt_{\overline{T}}$, n mi $(24\ h)^{-1}$]; and (e),(f) averaged intensification rates during the TC intensification periods [$dV/dt_{\overline{T}}$, kt $(24\ h)^{-1}$].

expansion rates and the LMF_{rot} orientations is not clear (Fig. 6d). It is presumably because such a relationship requires a convective asymmetry (or active rainbands) that is more common with at least moderate VWS magnitudes. Alternatively, significantly lower and higher intensification rates are associated with upshear and left-of-shear LMF_{rot} (Fig. 6f), respectively, for relatively weak VWS magnitudes. The higher intensification rates seem to explain the relatively small RV ratios for the TCs affected by left-of-shear LMF_{rot}.

In several studies regarding TC size and structure (Lee et al. 2010; Chan and Chan 2012; Chen et al. 2014a), the size parameter (e.g., the radius of 34-kt wind, R34) calculated directly from QuikSCAT surface wind was analyzed. Although the size data from the QuikSCAT and JTWC are technically not independent (JTWC estimates the R34 based on several observational platforms, including the QuikSCAT), the comparisons between the results based on the QuikSCAT size and on the JTWC size in those studies were able to strengthen their arguments. Therefore, the current study also examined the relationship between LMF_{rot} and the RV ratio that was calculated with R based on QuikSCAT observations and V from the JTWC best

TABLE 1. Results of two-sample t tests between the mean RV ratios from the two TC groups interacting with different LMF_{rot} orientations (i.e., R, U, L, and D) under two conditions: (top) VWS magnitudes $> 5.5\,m\,s^{-1}$ and (bottom) VWS magnitudes $< 5.5\,m\,s^{-1}$. The symbol + (−) represents that the mean RV ratio of the group indicated by the first column is significantly larger (smaller) than that of the group indicated by the first row at the 95% confidence level; the symbol ○ represents that the difference is not significant.

	R	U	L	D
VWS > 5.5 m s^{-1}				
R		○	+	○
U			+	○
L				−
D				
VWS < 5.5 m s^{-1}				
R		○	+	+
U			+	+
L				○
D				

track data. The QuikSCAT R was calculated following the methodology of Lee et al. (2010). As shown in Fig. 7a, the scatterplot of the JTWC R and the QuikSCAT R presents a positive correlation, with a correlation coefficient of 0.57.

Figure 7b examines the RV ratios calculated by QuikSCAT R and JTWC V. Since the QuikSCAT observation might not be available at the peak intensity of a TC, the analysis only includes TCs with a QuikSCAT R available during the last 24-h period of the intensification period. Consistent with Fig. 5a, TCs affected by right-of-shear LMF_{rot} have larger RV ratios, while the TCs affected by left-of-shear LMF_{rot} have significantly smaller RV ratios. However, the result based on the QuikSCAT R (Fig. 7b) shows an upward shift of the box plot for the upshear LMF_{rot} and a downward shift of the box plot for the downshear LMF_{rot}. These shifts could be attributed to a significantly larger R and smaller R obtained from QuikSCAT relative to JTWC for the TCs affected by upshear and downshear LMF_{rot}, respectively (Fig. 7c). Note also that based on similar examinations of two-sample t tests shown in Table 1, TCs affected by LMF_{rot}

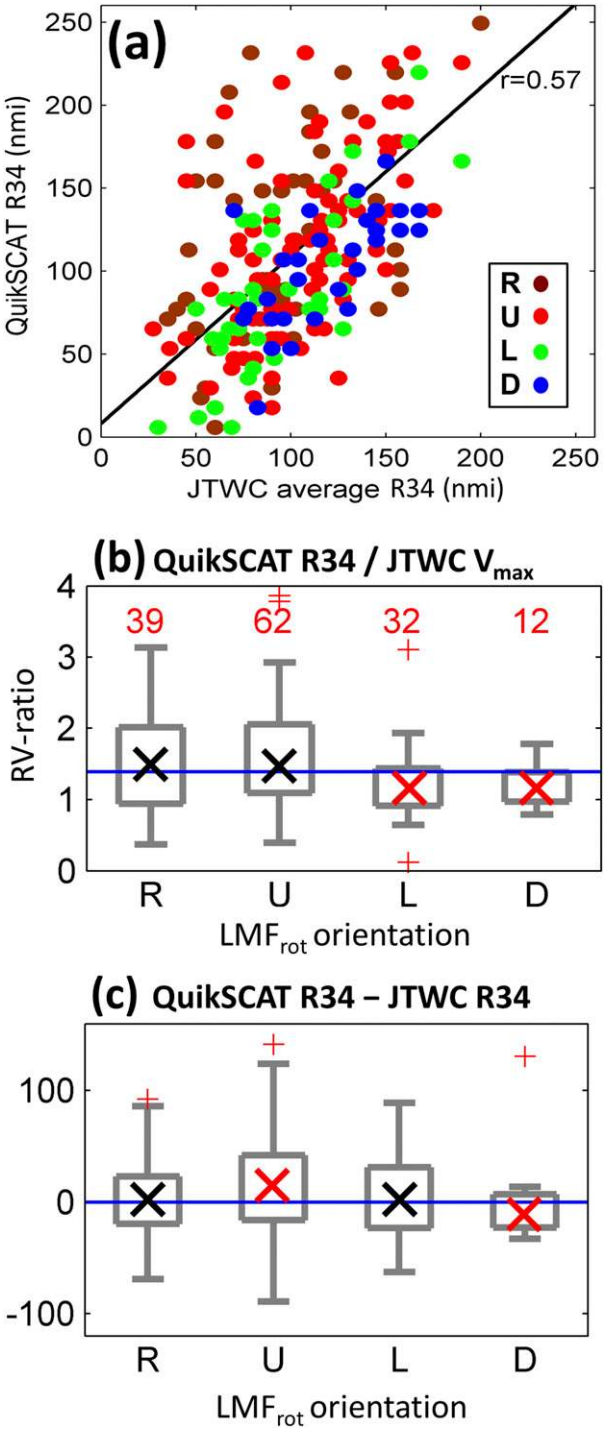

FIG. 7. (a) Scatterplot of radii of 34-kt wind estimated by JTWC (x axis; n mi) and radii of 34-kt wind calculated by QuikSCAT data (y axis; n mi). The least squares regression line and correlation coefficient for all samples are shown. Brown, red, green, and blue indicate TCs encountering right-of-shear, upshear, left-of-shear, and downshear LMF_{rot}, respectively. (b) As in Fig. 5a, but for RV ratio calculated by QuikSCAT R and JTWC V. (c) As in (b), but for the difference between QuikSCAT R and JTWC R.

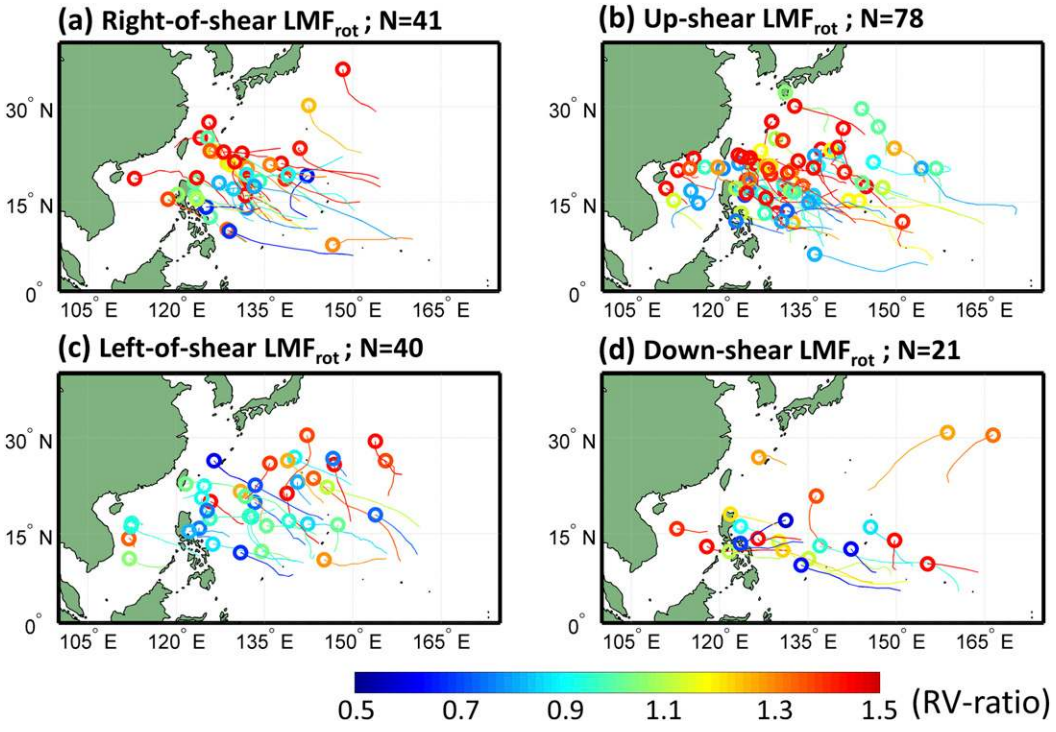

FIG. 8. Tracks of TCs affected by the four LMF_{rot} orientations. For each TC, only the track before the ending point of the intensification period is plotted. The color indicates the TC RV ratio.

with right-of-shear and upshear orientation have significantly larger RV ratios than TCs affected by left-of-shear and downshear LMF_{rot}. The analyses based on QuikSCAT *R* found a result generally consistent with the previous one.

c. *Synoptic environments setting up various LMF_{rot} orientations*

To increase the practical significance of this study to forecasters, this subsection relates the four LMF_{rot} orientations back to possible synoptic environments in which the TC is embedded. Figure 8 shows the TC tracks affected by the four LMF_{rot} orientations. In addition, following a similar method used to construct the CMORPH composite (section 2c), composite geopotential height, relative humidity, and wind at 850 hPa from the NCEP-FNL data for TCs affected by the four LMF_{rot} orientations were created (Fig. 9). Note, however, that these composites were rotated again to align the LMF_{rot} vector with the mean 850-hPa wind vector (see the red arrows in Fig. 9). Recall that in Fig. 3c, TCs affected by right-of-shear and upshear LMF_{rot} usually encountered south-southeasterly and southerly LMF, respectively, while TCs affected by left-of-shear and downshear LMF_{rot} usually encountered east-southeasterly LMF.

A TC affected by right-of-shear (Figs. 8a, 9a) or upshear LMF_{rot} (Figs. 8b, 9b) is likely to be associated with a monsoonal environment. Figures 8a and 8b show that these TCs are generally concentrated in the latitude range of 15°–22°N. Also, recall from Fig. 3b that most of the TCs in July and August (red dots in Fig. 3b) experienced right-of-shear and upshear LMF_{rot}. Also, the 850-hPa composites (Figs. 9a,b) further reveal that for the right-of-shear case (Fig. 9a), the moisture-rich monsoon trough extends far toward the west, and the TC is affected by a northeasterly VWS. On the other hand, for the upshear case (Fig. 9b), the monsoonal moisture is located to the southwest of the TC, and the TC is affected by a northerly VWS. Finally, the composite TC affected by the upshear LMF_{rot} is located along the western edge of the subtropical high (the anticyclonic circulation in Fig. 9b).

TCs affected by left-of-shear LMF_{rot} show a relatively wide latitude distribution, and many TCs are located north of 20°N (Fig. 8c). Also, visual inspection of the track color in Fig. 8c reveals that these TCs tend to have a relatively small RV ratio (see also Fig. 5). The 850-hPa composite (Fig. 9c) suggests that the relative humidity in the southwest quadrant is lower than that of the right-of-shear and upshear cases

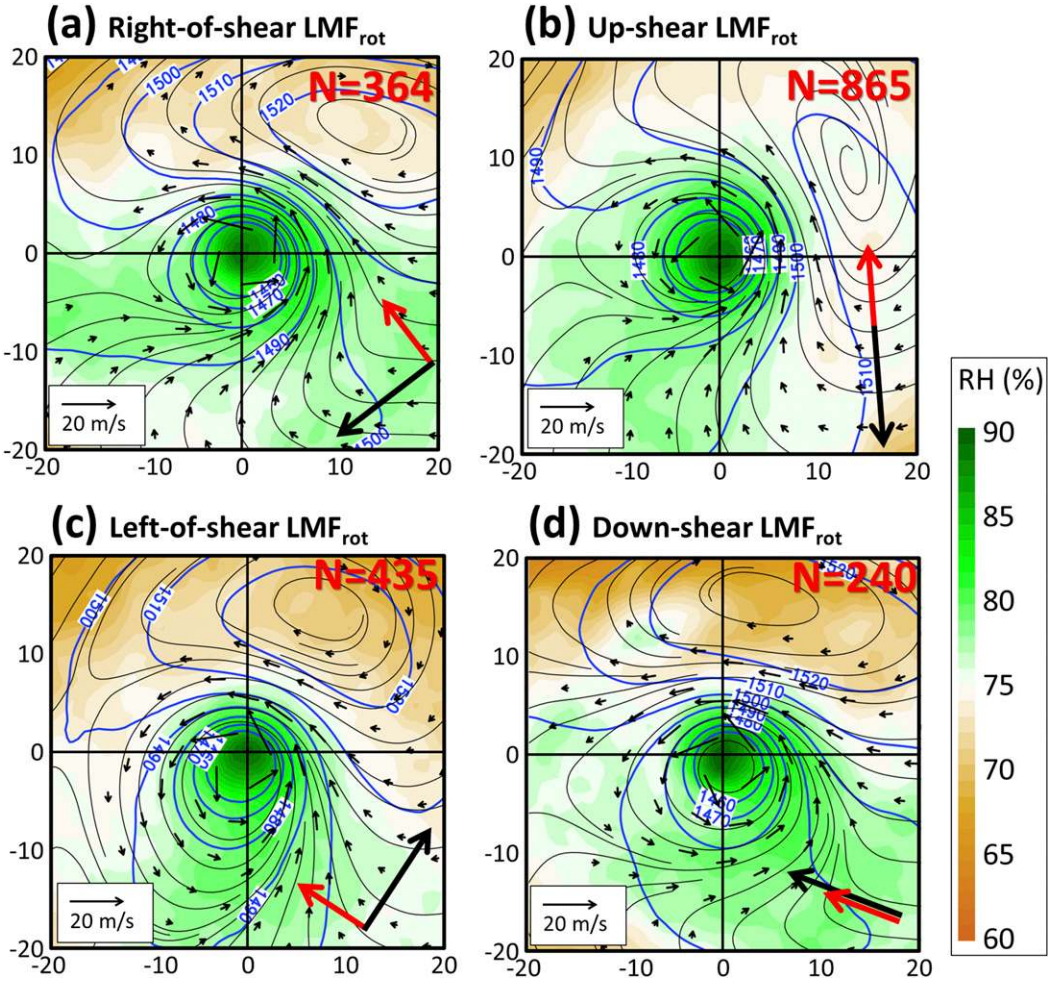

FIG. 9. Composites of relative humidity (color shading; %), height (blue contours; m), wind vectors (m s^{-1}; scale at the lower left of each panel), and streamlines at 850 hPa from the NCEP-FNL data on the rotated coordinates for TCs encountering LMF$_{rot}$ with (a) right-of-shear, (b) upshear, (c) left-of-shear, and (d) downshear orientations. Plotted at the lower right of each panel is a schematic showing the VWS (black) and the LMF$_{rot}$ (red) vector. Note that the composite is rotated to align the LMF$_{rot}$ vector with the mean 850-hPa wind vector of the corresponding composite samples. The units of *x* axis and *y* axis are degrees.

(Figs. 9a,b), and the TC is affected by a southwesterly VWS. Furthermore, the streamlines suggest a low-level synoptic flow pattern associated with easterly trade wind. Therefore, these TCs appear to be embedded in the environment where the monsoon trough is relatively shallow.

A TC affected by a downshear LMF$_{rot}$ (Figs. 8d, 9d) tends to be a late-season case (see also Fig. 3b) that moves toward the west at low latitudes south of 20°N (Fig. 8d). Figure 9d shows an area with high relative humidity in the southeast quadrant, coinciding with the confluence region between the TC circulation and the cross-equatorial flow.

In summary, this subsection reveals the associative relationship between certain LMF$_{rot}$ configurations and low-level synoptic environments. Specifically, whereas the composites of the right-of-shear and upshear groups resemble a monsoonal environment, the composite of the left-of-shear group is associated with easterly trade winds.

4. Effects of LMF$_{rot}$ orientation on the rainfall distribution and surface wind asymmetry

Following the steps described in section 2c, the composites of CMORPH rain rate and QuikSCAT surface wind were constructed. By analyzing these composites, the current section explores the asymmetric features of convection and surface wind. In addition, processes associated with these features are hypothesized to explain

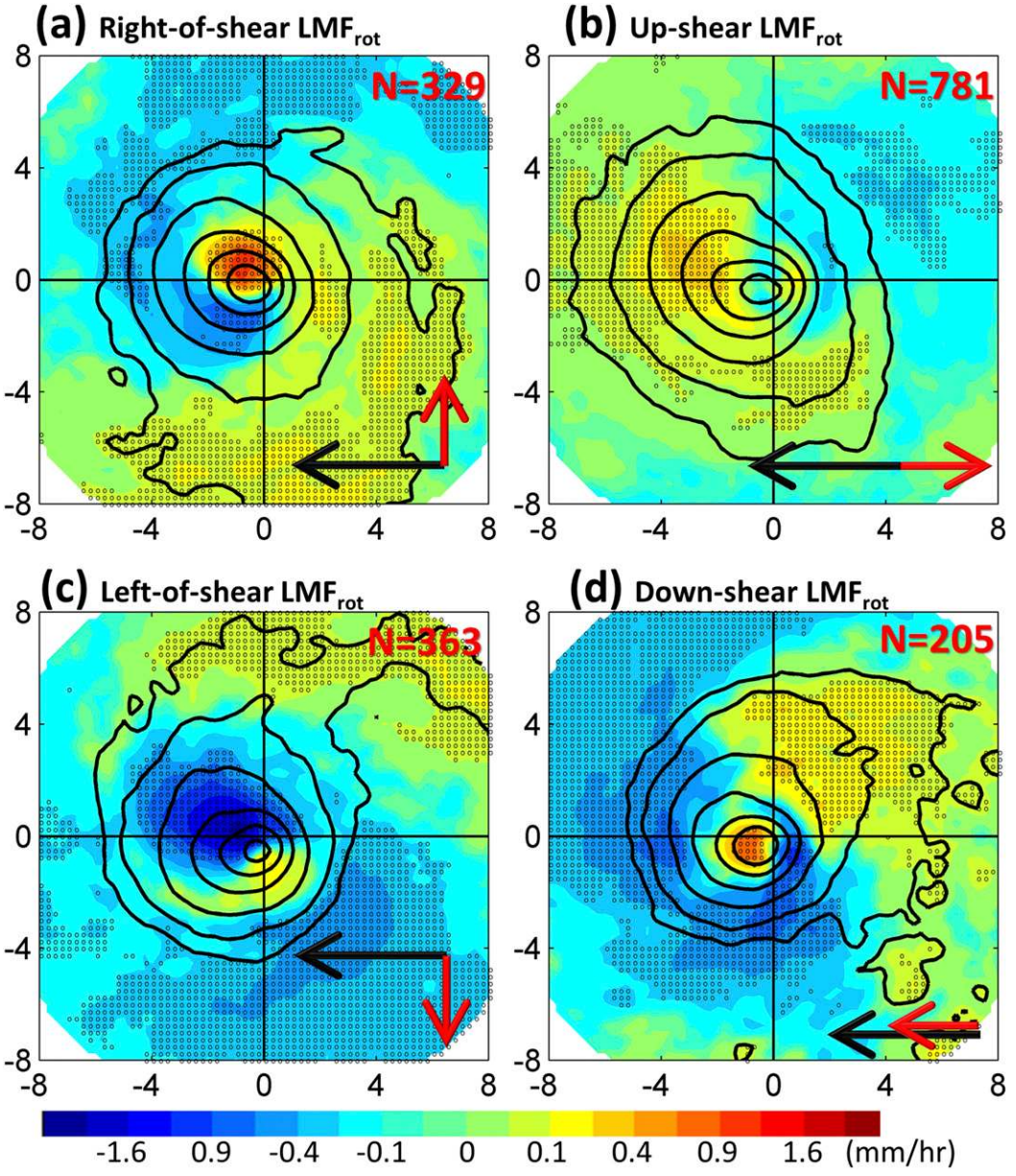

FIG. 10. Composites of CMORPH precipitation rate (contours at 0.5, 1, 2, 4, 6, and 8 mm h^{-1}) on rotated coordinates, in which the VWS vector is rotated toward the west, for the four LMF$_{rot}$ orientations. The shaded color indicates the rain-rate difference from the all-sample mean (color bar; mm h^{-1}). The dotted area represents where the rain rate significantly differs from the all-sample mean according to two-sample *t* tests. Plotted at the lower right of each panel is a schematic showing the VWS (black) and the LMF$_{rot}$ (red) vectors. The units of *x* axis and *y* axis are degrees. The sample number is shown at the upper-right corner of each panel.

the effects of LMF$_{rot}$ on the structural development of a vertically sheared TC.

a. TC rainfall asymmetry induced by the four LMF$_{rot}$ orientations

As shown in Fig. 10, CMORPH composites (the contours) for the four LMF$_{rot}$ orientations generally reveal downshear rainfall asymmetries induced by the TC–VWS interaction within radii of about 4°, which is consistent with previous studies (e.g., Corbosiero and Molinari 2003; Reasor et al. 2004; Riemer et al. 2010; Reasor et al. 2013). However, the different LMF$_{rot}$ orientations (red arrows plotted at the lower right of each panel) are also likely to modify the rainfall distributions based on the investigations of the CMORPH rain-rate differences between each composite and the

all-sample mean (shaded color in Fig. 10). First, whereas the upshear LMF_{rot} composite exhibits a larger area with positive rain-rate differences (the warm color in Fig. 10b), the left-of-shear composite exhibits a larger area with negative rain-rate differences (the cool color in Fig. 10c). This result suggests that a TC affected by a left-of-shear LMF_{rot} tends to have a smaller rainfall extent. As the distribution of the first available R of the left-of-shear group does not significantly differ from that of other groups (not shown), this small rain shield is attributed to the interaction between the TC and the left-of-shear LMF_{rot}. Furthermore, the small rain shield in part explains the relatively small RV ratio because the inactive rainbands are not favorable for the expansion of TC outer wind (Wang 2009).

Figure 10 also shows that for all composites, an enhanced rain rate in the outer region (i.e., beyond 3°) is present in the upstream semicircle with respect to the LMF_{rot}, while the enhanced rain rate within a 3° radius is presented in the downstream-left quadrant. This feature is particularly obvious for the right-of-shear and the downshear composites. Thus, for TCs affected by LMF_{rot} with right-of-shear orientations (Fig. 10a), rainfall is enhanced in the left-of-shear outer region and in the downshear-right rainband region. In contrast, for TCs affected by LMF_{rot} with left-of-shear orientations (Fig. 10c), rainfall is suppressed in the left-of-shear outer region and downshear-right rainband region.

Recall from section 3b that while the LMF_{rot} with a left-of-shear orientation favors intensification over expansion, the LMF_{rot} with a right-of-shear orientation favors expansion over intensification. Also, these two LMF_{rot} orientations are associated with the largest RV ratio differences. Thus, the rain-rate difference between the right-of-shear and the left-of-shear LMF_{rot} composites is evaluated. Figure 11 shows that the rain rate for the right-of-shear composite is significantly larger than that for the left-of-shear composite in the downshear-right rainband region (1°–3° from the center). This rain-rate difference suggests that TCs affected by right-of-shear LMF_{rot} have more rainband activity than TCs affected by left-of-shear LMF_{rot}. Wang (2009) showed that in an idealized model, active TC rainbands favor size expansion because of the additional heating from the rainband convection. Other studies (May and Holland 1999; Hill and Lackmann 2009) also suggested that rainbands may promote size expansion when the cyclonic potential vorticity is generated in the midtroposphere stratiform precipitation region. Therefore, the rain-rate difference between the right-of-shear and left-of-shear LMF_{rot} composites may explain the RV ratio differences. This result motivates further examination of the physical processes contributing to the different rainfall distributions associated with various LMF_{rot} orientations.

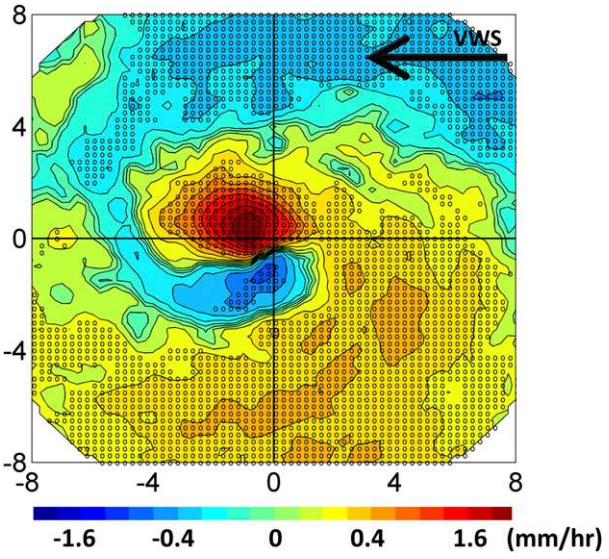

FIG. 11. The difference of CMORPH precipitation rate between the composite of TCs affected by right-of-shear and left-of-shear LMF_{rot}. The dotted area represents that where the means between the two composites significantly differ from each other at the 95% confidence level. The units of x axis and y axis are degrees.

b. *TC surface wind asymmetry induced by the four LMF_{rot} orientations*

QuikSCAT surface winds of TCs during 2003–09 were used to construct composites to investigate the TC surface wind asymmetry induced by the four LMF_{rot} orientations (see section 2c). As shown in Fig. 12, LMF_{rot} orientations dominate the asymmetry of both tangential wind and radial wind. For all four composites, tangential wind maxima are found on the right-hand side of the LMF_{rot} orientation due to the superposition of the low-level flows and the TC circulation (Figs. 12a,d,g,j). Also, Figs. 12b, 12e, 12h, and 12k suggest that the inward radial velocity is present in the upstream semicircle of the LMF_{rot}.

The surface flow with respect to the moving TC center is also examined. Although the radial velocity asymmetry locations are different among the four composites (Figs. 12b,e,h,k), the storm motion relative inflow locations for the various LMF_{rot} orientations are similar (Figs. 12c,f,i,l). Specifically, the storm motion relative inflow is present in the downshear quadrants for all four composites. In addition, assuming (i) a 2D flow and (ii) the pattern of storm motion relative flow does not quickly evolve at a time scale of about a day, the storm motion relative streamlines would be similar to the inflow trajectories. Thus, approximate trajectories were calculated based on the QuikSCAT composites, as discussed later in section 4c.

As the QuikSCAT composites suggest that the LMF_{rot} orientations are associated with the asymmetry of

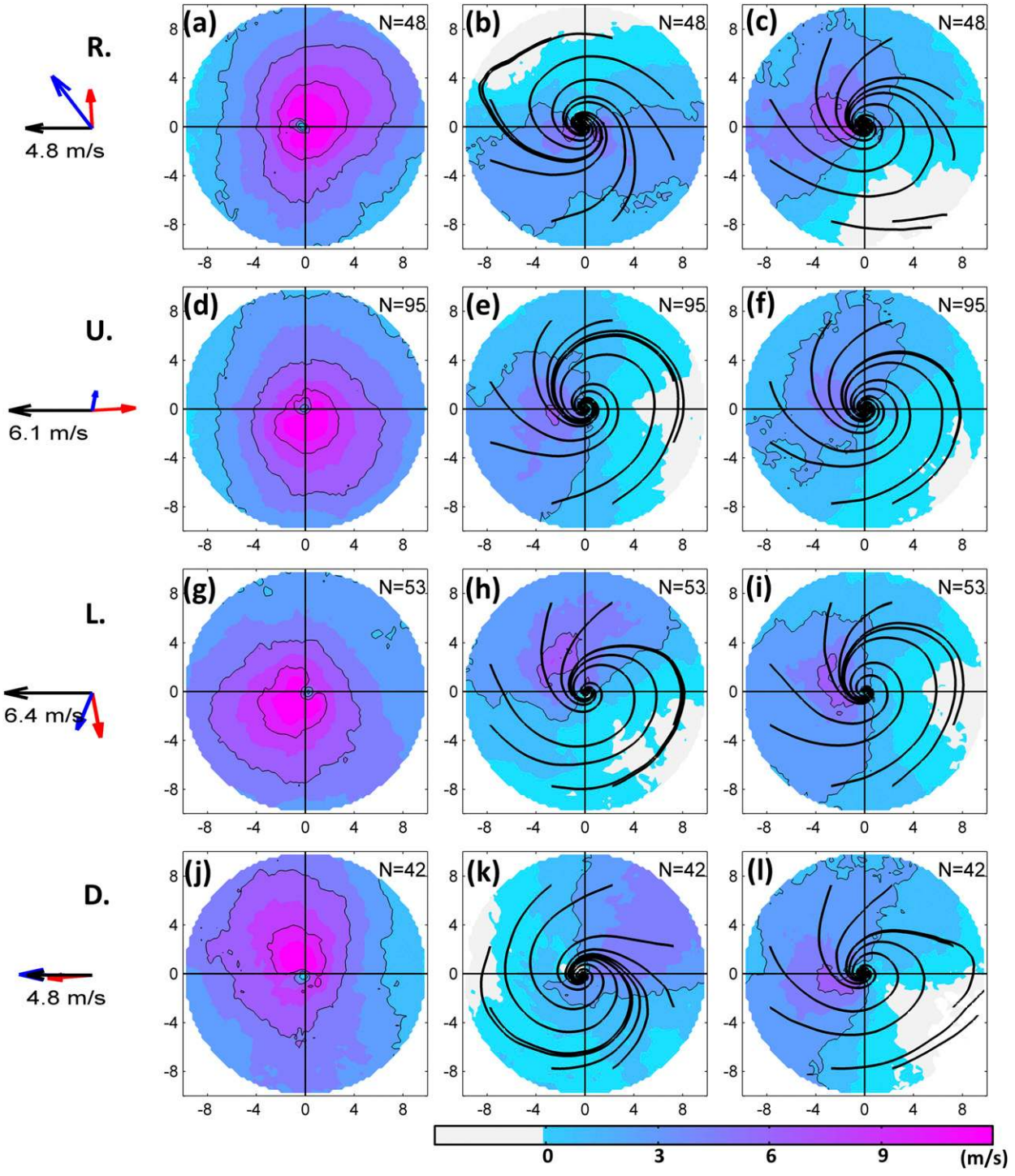

FIG. 12. Composites of QuikSCAT surface winds on rotated coordinates, in which the VWS vector is rotated toward the west. For TCs with a right-of-shear LMF_{rot} orientation, composites show (a) tangential wind velocity, (b) streamlines and radial wind velocity toward the TC center, and (c) streamlines and radial inflow relative to the moving TC center. Plotted at the left are the averaged rotated VWS vectors with the magnitude (black; m s^{-1}), averaged LMF_{rot} vector (red; m s^{-1}), and averaged TC motion vector (blue; m s^{-1}). (d)–(l) As in (a)–(c), but for TCs encountering LMF_{rot} with (d)–(f) upshear (U), (g)–(i) left-of-shear (L), and (j)–(l) downshear (D) orientations. The units of *x* axis and *y* axis are degrees. The sample number is shown at the upper-right corner of each panel.

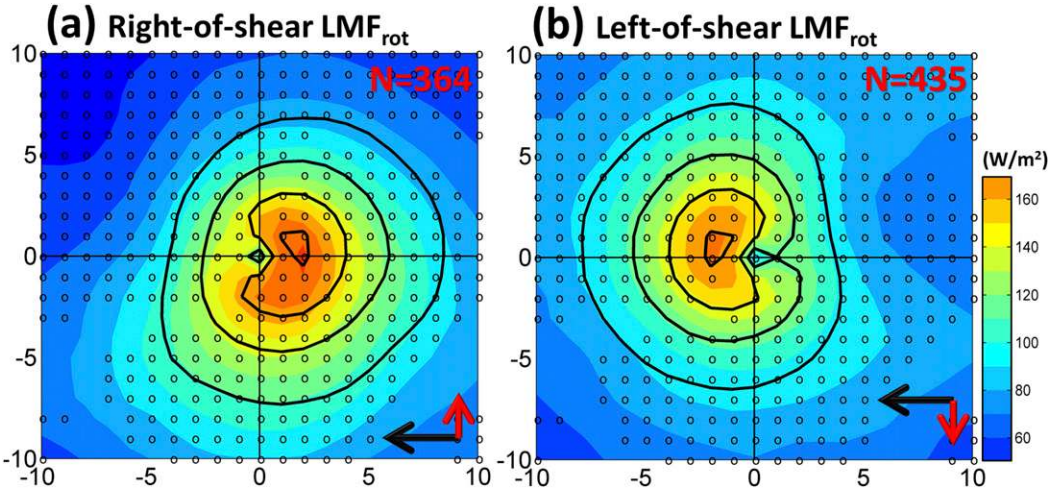

FIG. 13. Composites of surface latent heat flux (shaded, W m^{-2}) and surface wind speed (contoured at 8, 10, 12, and 14 m s^{-1}) from the NCEP-FNL data for the TCs encountering LMF$_{rot}$ with (a) right-of-shear and (b) left-of-shear orientations. The dotted area represents where the latent heat fluxes between the two composites significantly differ from each other. Plotted at the lower right of each panel is a schematic showing the VWS (black) and the LMF$_{rot}$ (red) vectors. The units of x axis and y axis are degrees. The sample number is shown at the upper-right corner of each panel.

ground-relative wind speed, it is proposed that the LMF$_{rot}$ affects the asymmetry of the air–sea enthalpy flux. Figure 13 examines the air–sea latent heat flux (LHF) for TCs affected by right-of-shear and left-of-shear LMF$_{rot}$ based on the NCEP-FNL composites. The methodology to construct the composites of surface wind speed and latent heat flux is similar to that of Figs. 8 and 10. Also, the LHF is calculated via the bulk formula

$$\mathrm{LHF} = L_v c_k \rho_d U_{10} (q^*_{\mathrm{SST}} - q),$$

where L_v is the latent heat of vaporization, c_k is the enthalpy exchange coefficient, ρ_d is the dry air density, U_{10} is the 10-m wind speed, q^*_{SST} is the saturated specific humidity at SST, and q is the 2-m specific humidity. These variables are directly taken from or derived based on the NCEP-FNL dataset. Composites of latent heat flux suggest that the flux differences between the composites are highly dependent on differences in the surface wind speed. Whereas the positive latent heat flux asymmetry is present on the upshear side of the right-of-shear composite (Fig. 13a), the positive latent heat flux asymmetry is present in the downshear side of the left-of-shear composite (Fig. 13b).

c. *Hypothesized processes of TC structure development associated with shear-relative LMF$_{rot}$*

Figure 14 shows that the enhanced rainfall in the rainband region (1°–3° from the center) for the right-of-shear case is strong and concentrated in the downshear-right quadrant (Fig. 14, red contour). Also, compared with the right-of-shear case, the area with high rain rate for the left-of-shear composite (Fig. 14b, lightly shaded area) is cyclonically shifted toward the left-of-shear side, leading to a more axisymmetric convective feature.

To explain the enhanced rainfall in the rainband region for the right-of-shear composite, we propose a conceptual model based on approximate flow trajectories and the distinct latent heat flux asymmetries (proportional to the surface wind speed; black contours in Fig. 14). These approximate trajectories were computed with respect to the moving TC center from the QuikSCAT composites (black lines in Fig. 12c,i), assuming two-dimensional flow. As such, the trajectories should be interpreted as a schematic representation of the flow. As shown in Fig. 14, three backward trajectories are released in the downshear rainband region, while another three are released in the upshear inner core. The trajectories were computed over a 36-h period. As the boundary layer moisture distribution could not be easily estimated by composites based on available satellite remote sensing, the averaged latent heat flux along each trajectory (trajectory color in Fig. 14) is calculated based on the NCEP-FNL composites (Fig. 13). Extended analyses were done to confirm that the trajectory and flux calculated based on the composites generally agree with the averaged characteristics of trajectories and fluxes for each case that goes into the composite (not shown). What we propose below draws heavily on the published numerical simulations of Rappin and Nolan (2012). They suggested that for an upshear surface flow case, the relatively large surface latent heat flux in the left-of-shear area of high surface

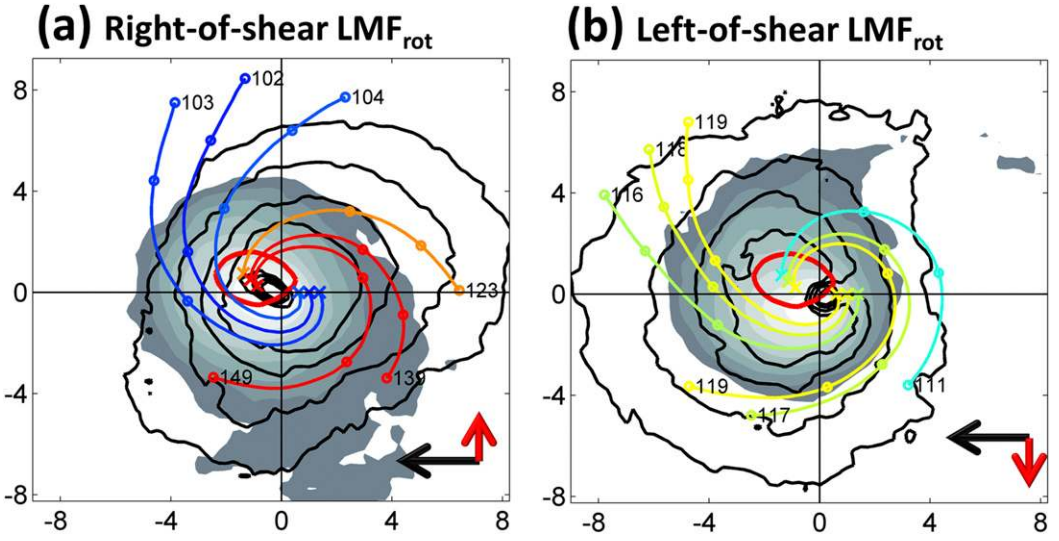

FIG. 14. Composite CMORPH rain rate (shaded from 0.5 to 10 mm h^{-1}), the difference in CMORPH composites between right-of-shear LMF$_{rot}$ and left-of-shear LMF$_{rot}$ (red contour at 0.8 mm h^{-1}), composite QuikSCAT surface wind speed (contoured at 8, 10, and 12 m s^{-1}), and approximated surface trajectories for the TCs affected by LMF$_{rot}$ with (a) right-of-shear and (b) left-of-shear orientations. These hypothesized backward trajectories are calculated based on the QuikSCAT composite of surface wind concerning the moving TC center (Figs. 12c,i). The parcels are released at positions indicated by ×; each circle indicates a 12-h interval; the text and color of each trajectory indicate the average of latent heat flux (W m^{-2}; see Fig. 13) along the trajectory. Plotted at the lower right of each panel is a schematic showing the VWS (black) and the LMF$_{rot}$ (red) vector. The units of *x* axis and *y* axis are degrees.

wind speed helps recover boundary layer moisture and promotes convection in the upshear-left quadrant.

For TCs affected by right-of-shear LMF$_{rot}$ (Fig. 14a), air parcels experiencing higher surface fluxes (higher average wind speed) along the trajectories in the upshear quadrants enter the downshear convective region (trajectories with warm colors in Fig. 14a), and air parcels experiencing lower surface fluxes along the trajectories in the downshear quadrant enter the upshear inner core (blue trajectories in Fig. 14a). This pattern of inferred surface fluxes would enhance the asymmetric rain rate that exists because of the vertical wind shear. The relatively strong rainfall asymmetry for the right-of-shear LMF$_{rot}$ case suggests active rainband development in the area and accounts for the large TC expansion rate and the large RV ratio. As suggested by previous studies (Wang 2009; May and Holland 1999; Hill and Lackmann 2009), the diabatic heating from rainband activity is hypothesized to broaden the TC warm core and expand TC size.

For TCs affected by left-of-shear LMF$_{rot}$ (Fig. 14b), air parcels experiencing moderate surface fluxes along the trajectories in the upshear quadrant enter the downshear rainband region, while air parcels experiencing comparably moderate surface fluxes in the downshear quadrants might promote convection in the upshear inner core. The combined effect of these two trajectory bundles leads to a more axisymmetric rainfall distribution that, in turn, promotes intensification. Specifically, a more axisymmetric convective distribution may lead to more efficient intensification. Nolan and Grasso (2003) and Nolan et al. (2007) used a three-dimensional framework to show the nonhydrostatic, unsteady, and symmetric response of a TC-like vortex to the evolving asymmetries. They found that the symmetric response to the azimuthally averaged heating was much larger than the symmetric response to the asymmetric heating. Also, recent observational studies (Nguyen et al. 2017; Fischer et al. 2018) have shown that more symmetric convection is associated with greater intensification rates, including rapid intensification.

5. Conclusions

This article explores the effects of shear-relative LMF on TC structural evolution based on observational and reanalysis datasets. TC structural evolution during the intensification period was estimated by the RV ratio, which simultaneously examines TC size and intensity. This parameter is defined as the ratio of a TC's maximum intensity and its radius of 34-kt wind at the ending point of the intensification period. Based on the analyses of 180 western North Pacific TCs, TCs with the RV ratios in the lowest quartile of all 180 samples favored

intensification over expansion, with 82% of these TCs experiencing rapid intensification; TCs with the RV ratios in the topmost quartile favored size expansion, with only 28% of these experiencing rapid intensification.

Among several environmental factors that may affect the RV ratio, this study highlights the role of LMF orientation with respect to the deep-layer VWS, referred to here as LMF_{rot}. The RV ratio is found to have a significant relationship with the LMF_{rot} orientation. Specifically, whereas an LMF directed toward the left-of-shear orientation favors TC intensification, a right-of-shear LMF favors size expansion.

To understand the interaction between the TC and LMF_{rot}, this study further analyzed the asymmetric surface flow and asymmetric rainfall distribution of TCs by QuikSCAT surface wind and CMORPH rain rate, respectively. The CMORPH composites reveal that active rainbands are likely to develop in the downshear-right quadrant for the TCs affected by right-of-shear LMF_{rot}, while rainbands are suppressed for the TCs affected by left-of-shear LMF_{rot}. Furthermore, a conceptual model (Fig. 14) regarding the asymmetric surface features induced by the different LMF_{rot} orientations is hypothesized to explain these different rainband behaviors, as well as the distinct structural evolutions of the vertically sheared TCs.

This conceptual model proposes that TC structural evolution is controlled by the interaction between (i) surface enthalpy flux associated with the surface wind maximum induced by TC–LMF interaction and (ii) flow trajectories with respect to the moving TC center, which are associated with the inflow in the downshear quadrants. Note that for all four LMF_{rot} orientations, the storm-relative inflow region is always located on the downshear side. Therefore, for a TC affected by an LMF_{rot} with a right-of-shear orientation, the air mass influenced by high-enthalpy fluxes in the upshear quadrant along the trajectory is transported into the downshear convective region, promoting the rainband development. On the other hand, for a TC affected by a left-of-shear LMF_{rot}, the air mass influenced by low-enthalpy fluxes in the upshear quadrant along the trajectory is transported into the downshear convective region, suppressing the rainband development. It is suggested that stronger rainfall asymmetry in the downshear rainband region for TCs affected by right-of-shear LMF_{rot} promotes TC size expansion due to the heating effects of rainbands (May and Holland 1999; Wang 2009; Hill and Lackmann 2009). In contrast, the more symmetric rainfall distribution for TCs affected by left-of-shear LMF_{rot} may favor intensification over expansion due to a better intensification efficiency (Nolan and Grasso 2003; Nolan et al. 2007).

The next phase of the current study will involve idealized Weather Research and Forecasting Model simulations to explore the physical processes accounting for the structural evolution of a vertically sheared TC. An advantage of using idealized model simulations is that the effect of LMF_{rot} on TC structure could be explored without the influence of other environmental factors, such as environmental humidity. Also, the simulated data allow the direct calculation of the trajectories and moisture budgets within the boundary layer. This work will not only validate the conceptual model explaining the TC rainfall distribution associated with the interaction between the LMF-related surface flux and storm motion relative inflow, but also explore the mesoscale processes and feedbacks associated with the rainband development attributed to distinct LMF_{rot} orientations.

Acknowledgments. The authors thank Jonathan Vigh of NCAR for his constructive comments to improve the manuscript. The calculations of environmental vertical wind shear were performed using the code provided by David Ahijevych of NCAR. High-performance computing resources and access to the RDA datasets were provided by NCAR's Computational Information Systems Laboratory. We also appreciate the help from two anonymous reviewers to significantly improve the manuscript. This work was funded by Grant 105-2917-I-564-013 of Ministry of Science and Technology, Taiwan, and the National Science Foundation under Cooperative Agreement AGS-1033112. The National Center for Atmospheric Research is sponsored by the National Science Foundation.

REFERENCES

Akter, N., and K. Tsuboki, 2012: Numerical simulation of Cyclone Sidr using a cloud-resolving model: Characteristics and formation process of an outer rainband. *Mon. Wea. Rev.*, **140**, 789–810, https://doi.org/10.1175/2011MWR3643.1.

Chan, K. T. F., and J. C. L. Chan, 2012: Size and strength of tropical cyclones as inferred from QuikSCAT data. *Mon. Wea. Rev.*, **140**, 811–824, https://doi.org/10.1175/MWR-D-10-05062.1.

——, and ——, 2014: Impacts of initial vortex size and planetary vorticity on tropical cyclone size. *Quart. J. Roy. Meteor. Soc.*, **140**, 2235–2248, https://doi.org/10.1002/qj.2292.

——, and ——, 2015: Impacts of vortex intensity and outer winds on tropical cyclone size. *Quart. J. Roy. Meteor. Soc.*, **141**, 525–537, https://doi.org/10.1002/qj.2374.

Chen, B.-F., C.-S. Lee, and R. L. Elsberry, 2014a: On tropical cyclone size and intensity changes associated with two types of long-lasting rainbands in monsoonal environments. *Geophys. Res. Lett.*, **41**, 2575–2581, https://doi.org/10.1002/2014GL059368.

——, R. L. Elsberry, and C.-S. Lee, 2014b: Origin and maintenance of the long-lasting, outer mesoscale convective system in

Typhoon Fengshen (2008). *Mon. Wea. Rev.*, **142**, 2838–2859, https://doi.org/10.1175/MWR-D-14-00036.1.

Corbosiero, K. L., and J. Molinari, 2002: The effects of vertical wind shear on the distribution of convection in tropical cyclones. *Mon. Wea. Rev.*, **130**, 2110–2123, https://doi.org/10.1175/1520-0493(2002)130<2110:TEOVWS>2.0.CO;2.

——, and ——, 2003: The relationship between storm motion, vertical wind shear, and convective asymmetries in tropical cyclones. *J. Atmos. Sci.*, **60**, 366–376, https://doi.org/10.1175/1520-0469(2003)060<0366:TRBSMV>2.0.CO;2.

Davis, C., and Coauthors, 2008: Prediction of landfalling hurricanes with the Advanced Hurricane WRF Model. *Mon. Wea. Rev.*, **136**, 1990–2005, https://doi.org/10.1175/2007MWR2085.1.

DeHart, J. C., R. A. Houze, and R. F. Rogers, 2014: Quadrant distribution of tropical cyclone inner-core kinematics in relation to environmental shear. *J. Atmos. Sci.*, **71**, 2713–2732, https://doi.org/10.1175/JAS-D-13-0298.1.

DeMaria, M., and J. Kaplan, 1994: A Statistical Hurricane Intensity Prediction Scheme (SHIPS) for the Atlantic basin. *Wea. Forecasting*, **9**, 209–220, https://doi.org/10.1175/1520-0434(1994)009<0209:ASHIPS>2.0.CO;2.

——, and ——, 1999: An updated Statistical Hurricane Intensity Prediction Scheme (SHIPS) for the Atlantic and eastern North Pacific basins. *Wea. Forecasting*, **14**, 326–337, https://doi.org/10.1175/1520-0434(1999)014<0326:AUSHIP>2.0.CO;2.

Dunion, J. P., and C. S. Velden, 2004: The impact of the Saharan air layer on Atlantic tropical cyclone activity. *Bull. Amer. Meteor. Soc.*, **85**, 353–366, https://doi.org/10.1175/BAMS-85-3-353.

Elsberry, R. L., and R. A. Jeffries, 1996: Vertical wind shear influences on tropical cyclone formation and intensification during TCM-92 and TCM-93. *Mon. Wea. Rev.*, **124**, 1374–1387, https://doi.org/10.1175/1520-0493(1996)124<1374:VWSIOT>2.0.CO;2.

Emanuel, K. A., C. DesAutels, C. Holloway, and R. Korty, 2004: Environmental control of tropical cyclone intensity. *J. Atmos. Sci.*, **61**, 843–858, https://doi.org/10.1175/1520-0469(2004)061<0843:ECOTCI>2.0.CO;2.

Finocchio, P. M., S. J. Majumdar, D. S. Nolan, and M. Iskandarani, 2016: Idealized tropical cyclone responses to the height and depth of environmental vertical wind shear. *Mon. Wea. Rev.*, **144**, 2155–2175, https://doi.org/10.1175/MWR-D-15-0320.1.

Fischer, M. S., B. H. Tang, K. L. Corbosiero, and C. M. Rozoff, 2018: Normalized convective characteristics of tropical cyclone rapid intensification events in the North Atlantic and eastern North Pacific. *Mon. Wea. Rev.*, **146**, 1133–1155, https://doi.org/10.1175/MWR-D-17-0239.1.

Frank, W. M., and E. A. Ritchie, 2001: Effects of vertical wind shear on the intensity and structure of numerically simulated hurricanes. *Mon. Wea. Rev.*, **129**, 2249–2269, https://doi.org/10.1175/1520-0493(2001)129<2249:EOVWSO>2.0.CO;2.

Galarneau, T. J., and C. A. Davis, 2013: Diagnosing forecast errors in tropical cyclone motion. *Mon. Wea. Rev.*, **141**, 405–430, https://doi.org/10.1175/MWR-D-12-00071.1.

Hence, D. A., and R. A. Houze, 2011: Vertical structure of hurricane eyewalls as seen by the TRMM Precipitation Radar. *J. Atmos. Sci.*, **68**, 1637–1652, https://doi.org/10.1175/2011JAS3578.1.

Hill, K. A., and G. M. Lackmann, 2009: Influence of environmental humidity on tropical cyclone size. *Mon. Wea. Rev.*, **137**, 3294–3315, https://doi.org/10.1175/2009MWR2679.1.

Holland, G. J., and R. T. Merrill, 1984: On the dynamics of tropical cyclone structural changes. *Quart. J. Roy. Meteor. Soc.*, **110**, 723–745, https://doi.org/10.1002/qj.49711046510.

Irish, J. L., D. T. Resio, and J. J. Ratcliff, 2008: The influence of storm size on hurricane surge. *J. Phys. Oceanogr.*, **38**, 2003–2013, https://doi.org/10.1175/2008JPO3727.1.

Jones, S. C., 1995: The evolution of vortices in vertical shear. I: Initially barotropic vortices. *Quart. J. Roy. Meteor. Soc.*, **121**, 821–851, https://doi.org/10.1002/qj.49712152406.

Joyce, R. J., J. E. Janowiak, P. A. Arkin, and P. Xie, 2004: CMORPH: A method that produces global precipitation estimates from passive microwave and infrared data at high spatial and temporal resolution. *J. Hydrometeor.*, **5**, 487–503, https://doi.org/10.1175/1525-7541(2004)005<0487:CAMTPG>2.0.CO;2.

Kaplan, J., and M. DeMaria, 2003: Large-scale characteristics of rapidly intensifying tropical cyclones in the North Atlantic basin. *Wea. Forecasting*, **18**, 1093–1108, https://doi.org/10.1175/1520-0434(2003)018<1093:LCORIT>2.0.CO;2.

Komaromi, W. A., and S. J. Majumdar, 2014: Ensemble-based error and predictability metrics associated with tropical cyclogenesis. Part I: Basinwide perspective. *Mon. Wea. Rev.*, **142**, 2879–2898, https://doi.org/10.1175/MWR-D-13-00370.1.

Lee, C. S., K. K. W. Cheung, W.-T. Fang, and R. L. Elsberry, 2010: Initial maintenance of tropical cyclone size in the western North Pacific. *Mon. Wea. Rev.*, **138**, 3207–3223, https://doi.org/10.1175/2010MWR3023.1.

——, C. C. Wu, T. C. C. Wang, and R. L. Elsberry, 2011: Advances in understanding the "perfect monsoon-influenced typhoon": Summary from International Conference on Typhoon Morakot (2009). *Asia Pac. J. Atmos. Sci.*, **47**, 213–222, https://doi.org/10.1007/s13143-011-0010-2.

——, B. F. Chen, and R. L. Elsberry, 2012: Long-lasting convective systems in the outer region of tropical cyclones in the western North Pacific. *Geophys. Res. Lett.*, **39**, L21812, https://doi.org/10.1029/2012GL053685.

Lin, I.-I., G. J. Goni, J. A. Knaff, C. Forbes, and M. M. Ali, 2013: Ocean heat content for tropical cyclone intensity forecasting and its impact on storm surge. *Nat. Hazards*, **66**, 1481–1500, https://doi.org/10.1007/s11069-012-0214-5.

Liu, K. S., and J. C. L. Chan, 1999: Size of tropical cyclones as inferred from *ERS-1* and *ERS-2* data. *Mon. Wea. Rev.*, **127**, 2992–3001, https://doi.org/10.1175/1520-0493(1999)127<2992:SOTCAI>2.0.CO;2.

Maclay, K. S., M. DeMaria, and T. H. Vonder Haar, 2008: Tropical cyclone inner-core kinetic energy evolution. *Mon. Wea. Rev.*, **136**, 4882–4898, https://doi.org/10.1175/2008MWR2268.1.

May, P. T., and G. J. Holland, 1999: The role of potential vorticity generation in tropical cyclone rainbands. *J. Atmos. Sci.*, **56**, 1224–1228, https://doi.org/10.1175/1520-0469(1999)056<1224:TROPVG>2.0.CO;2.

Nguyen, L. T., R. Rogers, and P. D. Reasor, 2017: Thermodynamic and kinematic influences on precipitation symmetry in sheared tropical cyclones: Bertha and Cristobal (2014). *Mon. Wea. Rev.*, **145**, 4423–4446, https://doi.org/10.1175/MWR-D-17-0073.1.

Nolan, D. S., and L. D. Grasso, 2003: Nonhydrostatic, three-dimensional perturbations to balanced, hurricane-like vortices. Part II: Symmetric response and nonlinear simulations. *J. Atmos. Sci.*, **60**, 2717–2745, https://doi.org/10.1175/1520-0469(2003)060<2717:NTPTBH>2.0.CO;2.

——, Y. Moon, and D. P. Stern, 2007: Tropical cyclone intensification from asymmetric convection: Energetics and efficiency. *J. Atmos. Sci.*, **64**, 3377–3405, https://doi.org/10.1175/JAS3988.1.

Onderlinde, M. J., and D. S. Nolan, 2014: Environmental helicity and its effects on development and intensification of tropical

cyclones. *J. Atmos. Sci.*, **71**, 4308–4320, https://doi.org/10.1175/JAS-D-14-0085.1.

Powell, M. D., and T. A. Reinhold, 2007: Tropical cyclone destructive potential by integrated kinetic energy. *Bull. Amer. Meteor. Soc.*, **88**, 513–526, https://doi.org/10.1175/BAMS-88-4-513.

Rappin, E. D., and D. S. Nolan, 2012: The effects of vertical shear orientation on tropical cyclogenesis. *Quart. J. Roy. Meteor. Soc.*, **138**, 1035–1054, https://doi.org/10.1002/qj.977.

Reasor, P. D., M. T. Montgomery, and L. D. Grasso, 2004: A new look at the problem of tropical cyclones in vertical shear flow: Vortex resiliency. *J. Atmos. Sci.*, **61**, 3–22, https://doi.org/10.1175/1520-0469(2004)061<0003:ANLATP>2.0.CO;2.

——, R. Rogers, and S. Lorsolo, 2013: Environmental flow impacts on tropical cyclone structure diagnosed from airborne Doppler radar composites. *Mon. Wea. Rev.*, **141**, 2949–2969, https://doi.org/10.1175/MWR-D-12-00334.1.

Ricciardulli, L., and F. Wentz, 2015: A scatterometer geophysical model function for climate-quality winds: QuikSCAT Ku-2011. *J. Atmos. Oceanic Technol.*, **32**, 1829–1846, https://doi.org/10.1175/JTECH-D-15-0008.1.

Riemer, M., 2016: Meso-β-scale environment for the stationary band complex of vertically sheared tropical cyclones. *Quart. J. Roy. Meteor. Soc.*, **142**, 2442–2451, https://doi.org/10.1002/qj.2837.

——, and M. T. Montgomery, 2011: Simple kinematic models for the environmental interaction of tropical cyclones in vertical wind shear. *Atmos. Chem. Phys.*, **11**, 9395–9414, https://doi.org/10.5194/acp-11-9395-2011.

——, ——, and M. E. Nicholls, 2010: A new paradigm for intensity modification of tropical cyclones: Thermodynamic impact of vertical wind shear on the inflow layer. *Atmos. Chem. Phys.*, **10**, 3163–3188, https://doi.org/10.5194/acp-10-3163-2010.

Sampson, C. R., P. A. Wittman, E. A. Serra, H. T. Tolman, J. Schauer, and T. Marchok, 2013: Evaluation of wave forecasts consistent with tropical cyclone warning center wind forecasts. *Wea. Forecasting*, **28**, 287–294, https://doi.org/10.1175/WAF-D-12-00060.1.

Shapiro, L. J., 1983: The asymmetric boundary layer flow under a translating hurricane. *J. Atmos. Sci.*, **40**, 1984–1998, https://doi.org/10.1175/1520-0469(1983)040<1984:TABLFU>2.0.CO;2.

Stenger, R. A., and R. L. Elsberry, 2013: Outer vortex wind structure changes during and following tropical cyclone secondary eyewall formation. *Trop. Cyclone Res. Rev.*, **2**, 184–195, https://doi.org/10.6057/2013TCRR04.02.

Tang, B., and K. Emanuel, 2010: Midlevel ventilation's constraint on tropical cyclone intensity. *J. Atmos. Sci.*, **67**, 1817–1830, https://doi.org/10.1175/2010JAS3318.1.

——, and ——, 2012: Sensitivity of tropical cyclone intensity to ventilation in an axisymmetric model. *J. Atmos. Sci.*, **69**, 2394–2413, https://doi.org/10.1175/JAS-D-11-0232.1.

Thomsen, G. L., R. K. Smith, and M. T. Montgomery, 2015: Tropical cyclone flow asymmetries induced by a uniform flow revisited. *J. Adv. Model. Earth Syst.*, **7**, 1265–1284, https://doi.org/10.1002/2015MS000477.

Wang, Y., 2009: How do outer spiral rainbands affect tropical cyclone structure and intensity? *J. Atmos. Sci.*, **66**, 1250–1273, https://doi.org/10.1175/2008JAS2737.1.

Willoughby, H. E., F. D. Marks, and R. J. Feinberg, 1984: Stationary and moving convective bands in hurricanes. *J. Atmos. Sci.*, **41**, 3189–3211, https://doi.org/10.1175/1520-0469(1984)041<3189:SAMCBI>2.0.CO;2.

Zhai, A. R., and J. H. Jiang, 2014: Dependence of US hurricane economic loss on maximum wind speed and storm size. *Environ. Res. Lett.*, **9**, 064019, https://doi.org/10.1088/1748-9326/9/6/064019.

Zhang, F., and D. Tao, 2013: Effects of vertical wind shear on the predictability of tropical cyclones. *J. Atmos. Sci.*, **70**, 975–983, https://doi.org/10.1175/JAS-D-12-0133.1.